Total Cross Section Measurements with π^-, Σ^- and Protons on Nuclei and Nucleons around 600 GeV/c

The SELEX Collaboration

U. Dersch [i], N. Akchurin [p], V.A. Andreev [k], A.G. Atamantchouk [k], M. Aykac [p], M.Y. Balatz [h], N.F. Bondar [k], A. Bravar [t], P.S. Cooper [e], L.J. Dauwe [q], G.V. Davidenko [h], G. Dirkes [i] A.G. Dolgolenko [h], D. Dreossi [t], G.B. Dzyubenko [h], R. Edelstein [c], L. Emediato [s], A.M.F. Endler [d], J. Engelfried [e,m], I. Eschrich [i,1], C.O. Escobar [s,2], A.V. Evdokimov [h], I.S. Filimonov [j,3], F.G. Garcia [s], M. Gaspero [r], S. Gerzon [ℓ], I. Giller [ℓ], V.L. Golovtsov [k], Y.M. Goncharenko [f], E. Gottschalk [c,e], P. Gouffon [s], O.A. Grachov [f,4], E. Gülmez [b], He Kangling [g], M. Iori [r], S.Y. Jun [c], A.D. Kamenskii [h], M. Kaya [p], J. Kilmer [e], V.T. Kim [k], L.M. Kochenda [k], K. Königsmann [i,5], I. Konorov [i,6], A.P. Kozhevnikov [f], A.G. Krivshich [k], H. Krüger [i], M.A. Kubantsev [h], V.P. Kubarovsky [f], A.I. Kulyavtsev [f,c], N.P. Kuropatkin [k], V.F. Kurshetsov [f], A. Kushnirenko [c], S. Kwan [e], J. Lach [e], A. Lamberto [t], L.G. Landsberg [f], I. Larin [h], E.M. Leikin [j], Li Yunshan [g], Li Zhigang [g], M. Luksys [n], T. Lungov [s,7], D. Magarrel [p], V.P. Maleev [k], D. Mao [c,8], Mao Chensheng [g], Mao Zhenlin [g], S. Masciocchi [i,9], P. Mathew [c,10], M. Mattson [c], V. Matveev [h], E. McCliment [p], S.L. McKenna [o], M.A. Moinester [ℓ], V.V. Molchanov [f], A. Morelos [m], V.A. Mukhin [f], K.D. Nelson [p], A.V. Nemitkin [j], P.V. Neoustroev [k], C. Newsom [p], A.P. Nilov [h], S.B. Nurushev [f], A. Ocherashvili [ℓ], G. Oleynik [e,8], Y. Onel [p], E. Ozel [p], S. Ozkorucuklu [p], S. Patrichev [k], A. Penzo [t], S.I. Petrenko [f], P. Pogodin [p], B. Povh [i], M. Procario [c], V.A. Prutskoi [h], E. Ramberg [e], G.F. Rapazzo [t], B.V. Razmyslovich [k], V.I. Rud [j], J. Russ [c], Y. Scheglov [i] P. Schiavon [t], V.K. Semyatchkin [h],

J. Simon [i], A.I. Sitnikov [h], D. Skow [e], V.J. Smith [o], M. Srivastava [s], V. Steiner [ℓ], V. Stepanov [k], L. Stutte [e], M. Svoiski [k], N.K. Terentyev [k,c], G.P. Thomas [a], L.N. Uvarov [k], A.N. Vasiliev [f], D.V. Vavilov [f], V.S. Verebryusov [h], V.A. Victorov [f], V.E. Vishnyakov [h], A.A. Vorobyov [k], K. Vorwalter [i,11], J. You [c], Zhao Wenheng [g], Zheng Shuchen [g], R. Zukanovich-Funchal [s]

[a] *Ball State University, Muncie, IN 47306, U.S.A.*

[b] *Bogazici University, Bebek 80815 Istanbul, Turkey*

[c] *Carnegie-Mellon University, Pittsburgh, PA 15213, U.S.A.*

[d] *Centro Brasiliero de Pesquisas Físicas, Rio de Janeiro, Brazil*

[e] *Fermilab, Batavia, IL 60510, U.S.A.*

[f] *Institute for High Energy Physics, Protvino, Russia*

[g] *Institute of High Energy Physics, Beijing, P.R. China*

[h] *Institute of Theoretical and Experimental Physics, Moscow, Russia*

[i] *Max-Planck-Institut für Kernphysik, 69117 Heidelberg, Germany*

[j] *Moscow State University, Moscow, Russia*

[k] *Petersburg Nuclear Physics Institute, St. Petersburg, Russia*

[ℓ] *Tel Aviv University, 69978 Ramat Aviv, Israel*

[m] *Universidad Autónoma de San Luis Potosí, San Luis Potosí, Mexico*

[n] *Universidade Federal da Paraíba, Paraíba, Brazil*

[o] *University of Bristol, Bristol BS8 1TL, United Kingdom*

[p] *University of Iowa, Iowa City, IA 52242, U.S.A.*

[q] *University of Michigan-Flint, Flint, MI 48502, U.S.A.*

[r] *University of Rome "La Sapienza" and INFN, Rome, Italy*

[s] *University of São Paulo, São Paulo, Brazil*

[t] *University of Trieste and INFN, Trieste, Italy*

Abstract

Total cross sections for Σ^- and π^- on beryllium, carbon, polyethylene and copper as well as total cross sections for protons on beryllium and carbon have been measured in a broad momentum range around 600 GeV/c. These measurements were performed with a transmission technique adapted to the SELEX hyperon-beam experiment at Fermilab. We report on results obtained for hadron-nucleus cross sections and on results for $\sigma_{\rm tot}(\Sigma^-{\rm N})$ and $\sigma_{\rm tot}(\pi^-{\rm N})$, which were deduced from nuclear cross sections.

1 Introduction

Hadronic total cross sections provide one measure of the strength of the hadronic interaction. They have been measured for a variety of reactions over a broad range of center of mass energies. These studies revealed that with increasing center of mass (CM) energy, hadron-hadron cross sections (generally) decrease to a minimum and then start rising again. An important current physics question is whether the rise of a specific hadron-hadron cross section is described by a power law in the CM energy. Addressing this question requires total cross-section experiments performed with a variety of hadronic projectiles, targets and energies covering the maximum possible range. However, for almost 20 years, there have been few new experiments in this field. Thus, important hadron-hadron cross sections as $\sigma_{\rm tot}(\pi{\rm p})$ and $\sigma_{\rm tot}({\rm Kp})$ are measured only up to 380 GeV/c and the total cross section $\sigma_{\rm tot}(\Sigma^-{\rm p})$ is only measured up to 137 GeV/c. At these maximum laboratory momenta only a first indication of the rise of these total cross sections is observed.

SELEX (Fermilab E781) is a fixed-target experiment at the Fermi National Accelerator Laboratory using a hyperon beam of about 600 GeV/c. The SELEX spectrometer, designed for spectroscopy of charm baryons, is well-suited to measure total cross sections with a transmission technique. It has excellent scattering-angle resolution, achieved by a system of silicon microstrip detectors.

SELEX does not have a liquid hydrogen target. Therefore, we measured the total hadron-nucleus cross sections $\sigma_{\rm tot}(\pi^-{\rm Be})$, $\sigma_{\rm tot}(\pi^-{\rm C})$, $\sigma_{\rm tot}(\pi^-{\rm CH_2})$, $\sigma_{\rm tot}(\Sigma^-{\rm Be})$, $\sigma_{\rm tot}(\Sigma^-{\rm C})$, $\sigma_{\rm tot}(\Sigma^-{\rm CH_2})$, $\sigma_{\rm tot}({\rm pBe})$ and $\sigma_{\rm tot}({\rm pC})$ with high precision. We then deduced the total cross sections $\sigma_{\rm tot}(\Sigma^-{\rm p})$ and $\sigma_{\rm tot}(\pi^-{\rm p})$ using both a CH_2 – C subtraction technique and a method based on the Glauber model to derive hadron-nucleon cross sections from hadron-nucleus cross sections.

Further, as data on hadron-nucleus cross sections are extremely scarce for

[1] Now at Imperial College, London SW7 2BZ, U.K.
[2] Current Address: Instituto de Física da Universidade Estadual de Campinas, UNICAMP, SP, Brazil
[3] deceased
[4] Present address: Dept. of Physics, Wayne State University, Detroit, MI 48201
[5] Now at Universität Freiburg, 79104 Freiburg, Germany
[6] Now at Physik-Department, Technische Universität München, 85748 Garching, Germany
[7] Current Address: Instituto de Física Teórica da Universidade Estadual Paulista, São Paulo, Brazil
[8] Present address: Lucent Technologies, Naperville, IL
[9] Now at Max-Planck-Institut für Physik, München, Germany
[10] Present address: Motorola Inc., Schaumburg, IL
[11] Present address: Deutsche Bank AG, 65760 Eschborn, Germany

charged projectiles, we also measured $\sigma_{\mathrm{tot}}(\pi^- \mathrm{Cu})$ and $\sigma_{\mathrm{tot}}(\Sigma^- \mathrm{Cu})$. All measurements were done during dedicated run periods in July 1997. Laboratory momenta range from 455 GeV/c to 635 GeV/c, the highest energy yet used for these studies.

2 Experimental setup

2.1 The hyperon beam

The hyperon beam is generated by selecting positively or negatively charged secondaries around 600 GeV/c that emerge from interactions of an 800 GeV/c primary proton beam with a beryllium production target. Its composition has not been completely measured. However, we have measured the main particle components of the event samples, which we selected to determine total cross sections (see section 5.2.1). This analysis shows that at the position of the total cross-section target the negative beam samples consist in average of $(52.5 \pm 1.6)\%$ mesons and $(47.5 \pm 1.6)\%$ baryons. Further, we measured a Ξ^- fraction of $(1.18 \pm 0.06)\%$ in these samples. Other baryonic fractions $(\overline{\mathrm{p}}, \Omega^-)$ were not measured, but empirical formulae (see [1]) predict they are less than 0.1%. Likewise, the K^- fraction of the negative beam is estimated with [1] to be $(1.6 \pm 1.0)\%$. Thus, we expect that the π^- fraction of the event samples is $(50.9 \pm 1.9)\%$.

In the event samples for positive beam we measured a meson fraction of $(8.1 \pm 1.4)\%$ and a baryon fraction of $(91.9 \pm 1.4)\%$. Furthermore, we measured a Σ^+ fraction of $(2.7 \pm 0.7)\%$. Using the empirical formula given in [1], we expect that the tiny meson fraction consists of 70% π^+ and 30% K^+.

From these compositions, one sees that as long as one can distinguish mesons from baryons (see section 2.2), the SELEX hyperon beam offers a unique possibility to measure total cross sections for protons, π^-, and Σ^- in a low contaminant environment.

2.2 The section of the SELEX spectrometer used for total cross-section measurements

The SELEX spectrometer is a 60 m long, 3 stage spectrometer. In total cross-section measurements, only its upstream detectors, shown in figure 1, are used.

The beam spectrometer placed in front of the target, is equipped with 12 silicon microstrip detectors to track incoming particles. The first 4 microstrip detectors (HSDs) have a resolution (pitch/$\sqrt{12}$) of 14.4 μm and a maximum

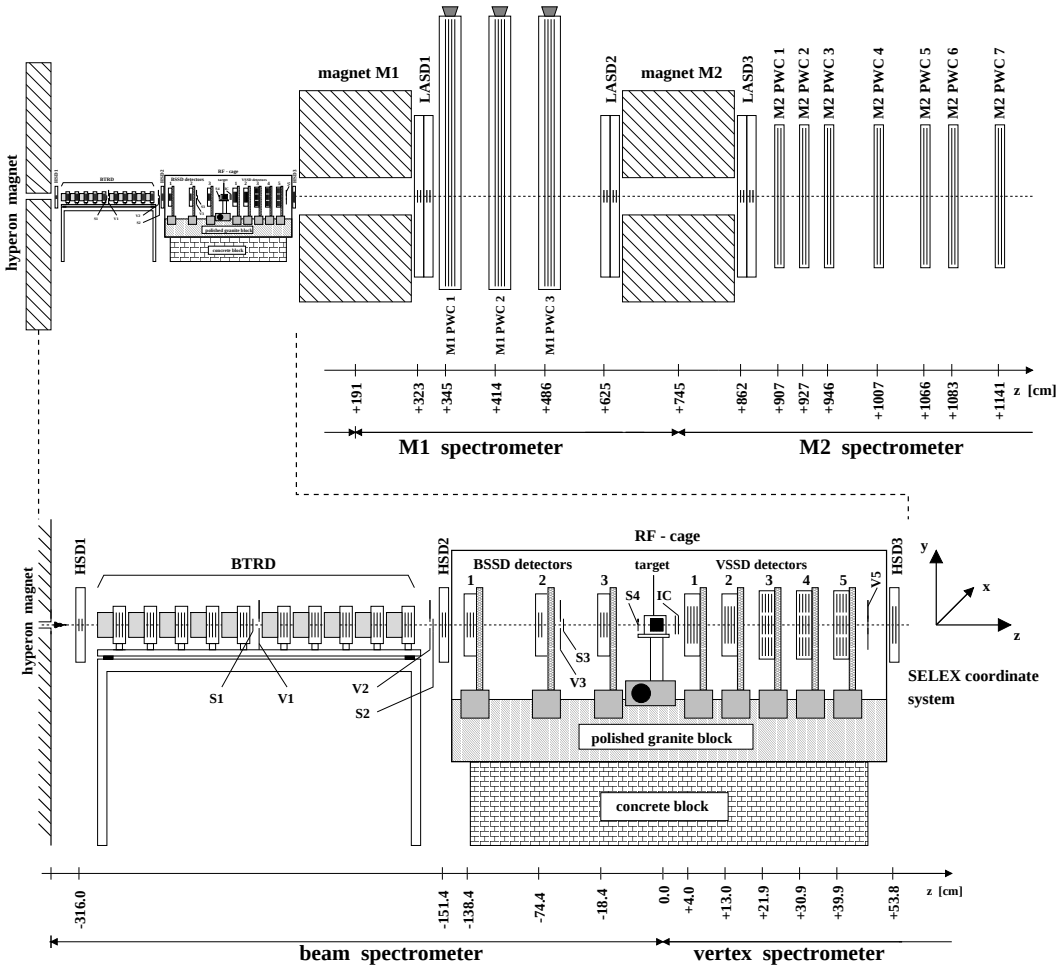

Fig. 1. Sections of the SELEX spectrometer involved in the measurement of total cross sections.

signal integration time of 100 ns. As this is the shortest integration time, but poorest spatial resolution, of all SELEX silicon microstrip detectors, the HSDs serve chiefly to reject stale tracks. Always, two HSDs are housed in a single station. The average efficiency of the HSDs is 92%.

The remaining 8 silicon microstrip detectors of the beam spectrometer are grouped into 3 stations (BSSDs) mounted on a granite block inside a noise shielded cage (RF-cage). These detectors have a resolution of 5.8 μm and an average efficiency of 99.6%.

Incoming particles are identified by a transition radiation detector (BTRD) with 10 separate transition radiation detector modules (TRMs). Each module is build of a radiator in succession with 3 proportional chambers (PCs) whose operating gas is a 70% Xe, 30% CO_2 mixture to optimize signal response time and to maximize absorption of transition-radiation photons. Each chamber has a single anode readout amplifier. A radiator consists of a stack of 200 polypropylene foils, each 17 μm thick and spaced at 500 μm.

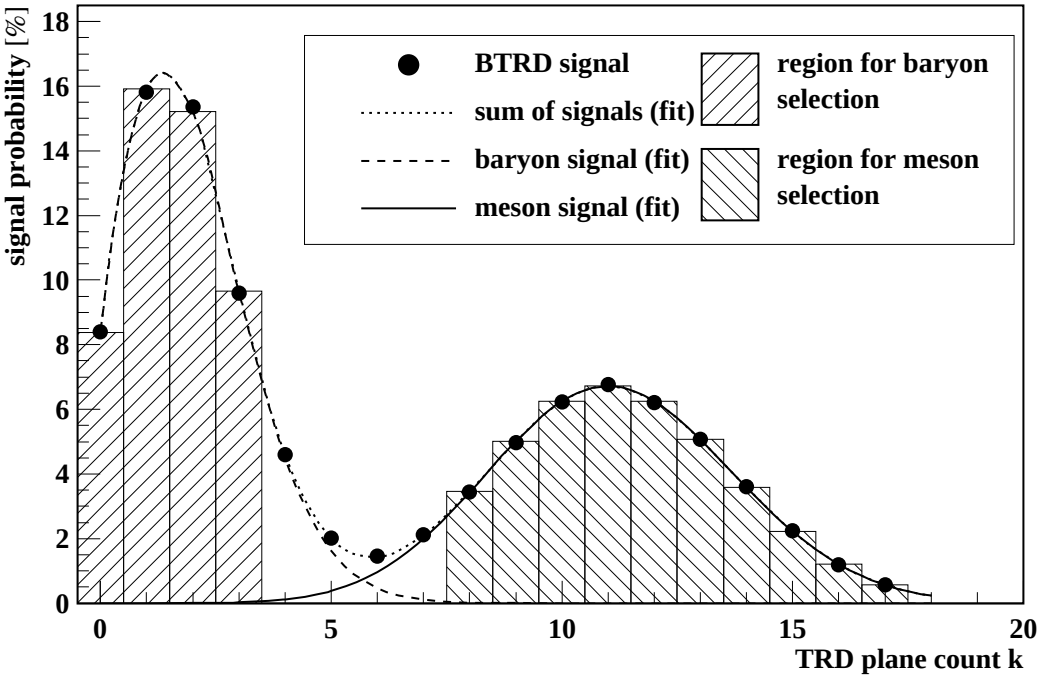

Fig. 2. A typical BTRD signal spectrum obtained for 600 GeV/c negatively charged secondaries.

Each BTRD PC gives a digital output when it detects an energy deposition above a fixed threshold. The sum of all PCs detecting a signal above threshold is the TRD plane count k. A typical probability spectrum of TRD plane counts, a BTRD signal spectrum, is shown in figure 2. It shows the baryon and meson responses at low and high TRD plane counts, respectively.

The signal components are separated by fitting the function:

$$p_{fit}(k) = \underbrace{\sum_{i=1}^{2} \kappa_i \binom{n}{k} p_i^k (1-p_i)^{n-k}}_{\text{baryon signal}} + \underbrace{\sum_{i=3}^{4} \kappa_i \binom{n}{k} p_i^k (1-p_i)^{n-k}}_{\text{meson signal}} \qquad (1)$$

to the normalized BTRD signal spectrum. Here, p_i and κ_i are fit-parameters with the constraints $1 = \kappa_1 + \kappa_2 + \kappa_3 + \kappa_4$ and p_1, $p_2 < p_3$, p_4 and n is the maximum possible TRD plane count. The fit-parameters p_i have the meaning of a PC response probability, when a meson (light particle) or baryon (heavy particle) passes. Thus, we obtain from (1) the meson fraction $(\kappa_3 + \kappa_4)$ and the baryon fraction $(\kappa_1 + \kappa_2)$ of the beam.

The target is followed by the vertex spectrometer, which consists of 22 silicon microstrip detectors grouped into 6 stations (VSSD1, ... , VSSD5 and HSD3). All VSSDs have a resolution of 5.8 μm, and except for one plane, which has a reduced efficiency of 68%, all others have an average efficiency of 98.8%. At the end of the vertex spectrometer, station HSD3 is mounted to the RF cage.

Although the total cross-section measurements presented in this article are

based only on detectors placed in the beam and the vertex spectrometer, we also use other parts of the SELEX apparatus to compute corrections. Further detectors involved in the analysis are situated in the M1 and the M2 spectrometer (see figure 1), which we describe briefly:

The M1 spectrometer starts at the center of the M1 magnet and ends at the center of the M2 magnet. For high resolution tracking of high energy particles in the central beam region, sets of 6 silicon microstrip detectors (LASD1 and LASD2) are mounted to the faces of the M1 and the M2 magnet. The LASD detectors have a resolution of 14.4 μm, and an average efficiency of 95.8%. For tracking outside the central beam region, 12 planes of wire chambers (PWCs) are installed.

The M2 spectrometer starts at the center of the M2 magnet. To enhance the momentum resolution for high energy particles, a third station of silicon microstrip detectors (LASD3) is mounted to the end face of the M2 magnet. This station is followed by 14 PWCs that are grouped into 7 stations (M2 PWC1, ..., M2 PWC7).

2.3 The targets

To optimize the precision, total cross-section measurements are done with special targets. Great care was taken in selecting and machining adequate target materials in order to obtain best chemical and mechanical properties (see table 1). All targets are thin such that multiple scattering, quantified by σ_θ of Molières' formula is significantly lower than the 25 μrad angular resolution provided by the beam and vertex spectrometer.

The carbon target is a stack of three quadratic pyrocarbon plates, each about 5 mm thick. Pyrocarbon is composed of thin carbon layers accumulated on top of each other in a high-temperature methane atmosphere. Compared to standard graphite it offers the advantages: no open porosity, a density close to that of a graphite monocrystal and less than 1 ppm (parts per million) non-carbon constituents. The beam faces of the carbon plates were milled with a diamond-powder liquid and oriented such that the beam faces of the stack are parallel to each other.

The polyethylene target is build from a high-purity polyethylene granulate with less than 1000 ppm contaminants. Molten granulate was solidified in a vessel, where great care was taken that no air bubbles penetrated. The material was then carefully machined to a target block, and beam faces were flattened using a diamond pin.

For the beryllium and the copper target, standard industry products of high purity are used.

target material	thickness L [mm] z-direction	transverse dimensions x [mm]	y [mm]	density ρ^* $[\frac{\mathrm{g}}{\mathrm{cm}^3}]$	σ_θ [μrad]	$\mathrm{X_{coll}}$ [%]
beryllium	50.92	30.7	51.2	1.848 ± 0.002	8.3	16.86
carbon	15.46	30.0	30.0	2.199 ± 0.003	6.0	5.40
polyethylene	40.86	30.0	25.0	0.9291 ± 0.0008	6.3	6.66
copper	1.00	30.0	30.0	8.96 ± 0.009	5.7	1.05

Table 1
Specifics of the targets used in total cross-section measurements. L: target thickness, ρ^*: density, σ_θ: expected spread in scattering angle due to multiple scattering calculated with Molières' formula for $\mathrm{p_{lab}} = 600\,\mathrm{GeV/c}$, X_{coll}: collision length.

2.4 Trigger and data acquisition

The SELEX trigger is a programmable four-stage trigger, designed to select events involving decays of charm hadrons in a high-intensity beam environment. The first 3 levels: T0, T1 and T2 are hardware triggers, whereas level T3 is an online software filter. In this section, we describe only the trigger as programmed for total cross-section data-taking.

At data-taking, the trigger accepted all beam events defined by the minimum-bias condition:

$$T0 \;=\; S1 \wedge S2 \wedge S3 \wedge \overline{V1} \wedge \overline{V2} \wedge \overline{V3}\;. \qquad (2)$$

S1, S2 and S3 are scintillation counters, and V1, V2 and V3 are veto counters to reject beam halo (see figure 1). In definition (2), a T0-pulse indicates a particle traversing the beam spectrometer in the direction of the target beam face. Thereby, the transverse trigger acceptance is constrained to the size of the rectangular hole in V2 ($12.8\,\mathrm{mm} \times 12.8\,\mathrm{mm}$).

In order to keep the minimum bias condition provided by the definition of T0, no information of detectors placed downstream of the experiment target influenced the spectrometer readout. Thus, each T0-pulse passed the T1 trigger level unbiased, and generated a T2-pulse, which started the spectrometer readout. The online software filter (level T3) was not used for total cross-section data-taking. Pulses of all trigger levels were counted by scalers for each spill, and saved in a trigger log file.

The SELEX trigger controlled readout and reset of the silicon-detector system, the basic tool in our total cross-section measurements. Except for the HSDs, all other silicon detectors use an SVX-I chip technology for data readout [2]. SVX chips are controlled by a sequencer SRS (silicon readout sequencer)

that interacts very closely with the trigger. First, it keeps the silicon detectors sensitive (for about $5\,\mu s$ effective integration time) and starts the chip read-out when receiving a T2-pulse. Second, the SRS resets the SVX-chips, when a silicon-clear signal arrives. Thereby, the silicon-clear signal is generated in the trigger logic through:

$$\text{Silicon clear } = V5_{\text{mult}} \ \vee \ C_{\text{pulser}} \ \vee \ (T1 \ \wedge \ \overline{T2}) \ . \tag{3}$$

Here, C_{pulser} are pulses from a gate generator running at a frequency of 20 kHz and $V5_{\text{mult}}$ represents pulses generated, when the V5 veto counter (see figure 1) detects a high multiplicity event. The condition $(T1 \wedge \overline{T2})$ was irrelevant for total cross-section data.

2.5 Experimental conditions and recorded data

During the fixed-target run 1996/97, the TEVATRON was operated in 60 s cycles with a spill time of 20 s. Data for total cross sections were taken during dedicated periods, with optimized experimental conditions for this measurement.

By adjusting the flux of the 800 GeV/c proton beam, the T0-rate was optimized to run the SELEX DAQ near, but safely below its capacity limit of $5{\cdot}10^4$ particles per spill. The low hyperon-beam flux allowed a high silicon-clear rate, which resulted in a very low-noise condition for the silicon-detector system and a low probability for stale tracks.

During data-taking, the M1 magnet was switched off to obtain a 2.5 m field- and material-free section, serving as fiducial region for precise reconstruction of hyperon decays. Magnet M2 was operated with a transverse momentum kick of $p_T^{M2} = 0.84\,\text{GeV/c}$.

At data-taking start, after mounting an experiment target in the RF-cage, an alignment RUN was taken to account for eventual detector displacements caused during the target installation. Then, the position of the experiment target was alternated every 30 min between its out and in-beam position. Thus, almost equal amounts of data were taken with full and empty target. A RUN, started after each target-position change, comprised typically 10^6 events. A total of $9.8{\cdot}10^7$ minimum-bias events were recorded with negative beam for the targets Be, C, Cu and CH_2. With positive beam, $3.0{\cdot}10^7$ minimum-bias events were written using the targets Be and C.

3 The principle of the transmission method

In contrast to scattering experiments, where $\sigma_{\rm tot}$ is deduced from a measured scattering angle distribution, in a transmission experiment $\sigma_{\rm tot}$ is deduced from the number of unscattered projectiles. Strictly, unscattered means zero scattering angle, but experimental resolution and Coulomb scattering limit this to a determination of the number of projectiles scattered by an angle θ, which is smaller than a maximum angle parameter $\theta_{\rm max}$ ($\mathrm{F_o}(<\theta_{\rm max})$). Thus, one infers the number of unscattered particles by extrapolating $\mathrm{F_o}(<\theta_{\rm max})$ to $\theta_{\rm max}=0$.

A standard transmission experiment consists of three elements: beam monitor, target, and transmission counter. The number of projectiles hitting the target under full-target (empty-target) condition $\mathrm{F_o}$ ($\mathrm{E_o}$) is counted by the beam monitor placed in front of the target. A transmission counter, placed downstream of the target, counts the corresponding number of projectiles $\mathrm{F_{tr}}(<\Omega_{\rm i})$ ($\mathrm{E_{tr}}(<\Omega_{\rm i})$), leaving the target within the maximum solid angles Ω_1 ... $\Omega_{\rm N}$. Recorded counts are combined to a set of partial cross sections $\sigma_{\rm part}(<\Omega_{\rm i})$, defined as:

$$\sigma_{\rm part}(<\Omega_{\rm i}) \;=\; \frac{1}{\rho L}\log\left[\frac{\mathrm{F_o}}{\mathrm{F_{tr}}(<\Omega_{\rm i})}\frac{\mathrm{E_{tr}}(<\Omega_{\rm i})}{\mathrm{E_o}}\right] \qquad \text{with} \quad \rho=\frac{\mathrm{N_A}\rho^*}{A}\;, \quad (4)$$

where ρ is the density of scattering centers in the target, A is the atomic mass and $\mathrm{N_A}$ is Avogadro's number.

Driving our choice of a transmission method is an important technical advantage of equation (4). We do not need to know absolute efficiencies of the beam and the transmission monitor. Their absolute values will cancel in (4) as long as they remain unchanged between and during the full- and the empty-target RUNs (stability condition).

Taking into account the event correlations between $\mathrm{F_o}$ ($\mathrm{E_o}$) and $\mathrm{F_{tr}}(<\Omega_{\rm i})$ ($\mathrm{E_{tr}}(<\Omega_{\rm i})$), the statistical error of a partial cross section is given by:

$$\delta\sigma_{\rm part}(<\Omega_{\rm i}) \;=\; \frac{1}{\rho L}\sqrt{\frac{1}{\mathrm{F_{tr}}(<\Omega_{\rm i})}-\frac{1}{\mathrm{F_o}}+\frac{1}{\mathrm{E_{tr}}(<\Omega_{\rm i})}-\frac{1}{\mathrm{E_o}}}\;. \qquad (5)$$

In a thin target approximation ($\rho L\sigma_{\rm tot}\ll 1$), a partial cross section $\sigma_{\rm part}(<\Omega_{\rm i})$ is related to the total hadronic cross section $\sigma_{\rm tot}$ (see e.g. [3]) by:

$$\sigma_{\rm tot}=\sigma_{\rm part}(<\Omega_{\rm i}) \;\underbrace{-\int\limits_{\Omega_{\rm i}}^{4\pi}\left(\frac{d\sigma}{d\Omega}\right)_{\rm C}d\Omega \;-\int\limits_{\Omega_{\rm i}}^{4\pi}\left(\frac{d\sigma}{d\Omega}\right)_{\rm CN}d\Omega}_{\text{Correction for C and CN scattering}}$$

$$+ \underbrace{\int_0^{\Omega_i} \left(\frac{d\sigma}{d\Omega}\right)_{el}^{hadr} d\Omega}_{\text{elastic term}} + \underbrace{\int_0^{\Omega_i} \left(\frac{d\sigma}{d\Omega}\right)_{inel}^{hadr} d\Omega}_{\text{inelastic term}} . \quad (6)$$

In equation (6), σ_{tot} is infered by first correcting partial cross sections for Coulomb scattering (C) and the Coulomb hadronic interference (CN) and then extrapolating to zero solid angle.

4 Data analysis

4.1 Data selection

In general, total cross-section data taken for a specific target were subject to varying experimental conditions: thresholds on silicon microstrip detectors, high voltages for trigger scintillators, and the inclination angle between primary proton beam and production target. Therefore, data belonging to a cross-section measurement with a specific target were divided into as many data sets as differing conditions had to be taken into account. This offered the possibility to calculate corrections and errors specifically for each experimental condition in a later stage of the analysis. To preserve the stability condition mentioned in chapter 3, a spill by spill data pre-selection was performed. Data of a spill or a whole run were rejected:

(1) When the experimental conditions concerning the functionality of the spectrometer (detector efficiencies, trigger performance and track reconstruction efficiencies) suddenly changed.
(2) When it was not possible to synchronize raw data with information in the trigger log file.
(3) When the BTRD showed instabilities or when the beam phase space lay outside the BTRD fiducial region.

4.2 Event selection for normalization

The total cross-section determination is made by counting how many good beam tracks are removed from the beam by interactions in the target. The normalization therefore depends only on the number of good beam tracks, which are identified by a software decision routine. This routine reconstructs tracks in the beam spectrometer using the HSD and BSSD hit information. It preserves the minimum-bias condition for the selected data by strictly avoiding event-selection rules that require information from detectors placed downstream of

the target. An event is accepted when it is possible to reconstruct a track called a "norm track", provided that the following properties are satisfied:

(1) Not more than a total of 150 hits in all BSSDs.
(2) At least 6 hits from BSSD planes along the track.
(3) At least one hit from an HSD plane along the track (HSD-tagging).
(4) A reduced track-fit χ^2 below 3.
(5) An extrapolated origin of the track at the known transverse position of the primary production target.
(6) Track intercept and slope parameters within the beam phase space accepted by magnetic collimation.
(7) A transverse track position at the longitudinal position of the experimental target, which is inside the trigger acceptance window and inside BTRD acceptance.
(8) A beam momentum assigned to the track, which is $\pm$ 100 GeV/c around the center of gravity value of the momentum spectrum.

Condition 3 rejects stale tracks. The selection rules 4 – 6 remove events in which hyperons decay before reaching the experiment target or react with detector material in the beam spectrometer. Constraint 7 assures also that selected tracks point to the mid-part of the experiment target face, where the best mechanical accuracy is obtained.

All listed conditions were true for about 50% of the selected events. From the resulting set of norm tracks for full- and empty-target conditions, we establish classes of BTRD-tagged norm tracks. This is done by introducing cuts on the BTRD information as indicated in figure 2 to separate baryonic and mesonic norm tracks. We then determine the corresponding normalization counts F_o and E_o by summing the norm tracks over the appropriate signal region.

4.3 Transmission counting

When a norm track is found in the event, we reconstruct a single track in the vertex spectrometer, which is leaving the interaction target at small angle with respect to the norm track.

The single-track algorithm was efficient and fast. It used hits of HSD3 to remove stale tracks. With loose cuts on the track parameters 98% of the norm tracks got assigned a track in the vertex spectrometer. Such vertex tracks were finally accepted as "transmitted tracks", when:

(1) There are at least 15 hits from VSSDs found within a track search corridor.
(2) The reduced track-fit χ^2 is below 3.

For each transmitted track, the scattering angle θ between norm and transmitted track is calculated. Following the idea of [4], a four-momentum transfer t is assigned to the event using the small angle approximation $t \approx -\mathrm{p}_{\mathrm{beam}}^2\theta^2$, where $\mathrm{p}_{\mathrm{beam}}$ is the momentum of the incoming particle. Transmitted tracks are assigned to t bins of width $5.0 \cdot 10^{-4}\,\mathrm{GeV}^2/\mathrm{c}^2$. Note that we count transmitted tracks in t-bins, rather than in bins of solid angle Ω as discussed in chapter 3. Summing the events in the t-bins from zero up to a maximum t_{i} leads to sets of transmission counts $\mathrm{F}_{\mathrm{tr}}(< |t_{\mathrm{i}}|)$ and $\mathrm{E}_{\mathrm{tr}}(< |t_{\mathrm{i}}|)$.

4.4 Spectra of uncorrected partial cross sections

Using the counts F_{o}, E_{o}, $\mathrm{F}_{\mathrm{tr}}(< |t_{\mathrm{i}}|)$, $\mathrm{E}_{\mathrm{tr}}(< |t_{\mathrm{i}}|)$ and the mechanical properties of the targets, partial cross sections $\sigma_{\mathrm{part}}(< |t_{\mathrm{i}}|)$ are calculated according

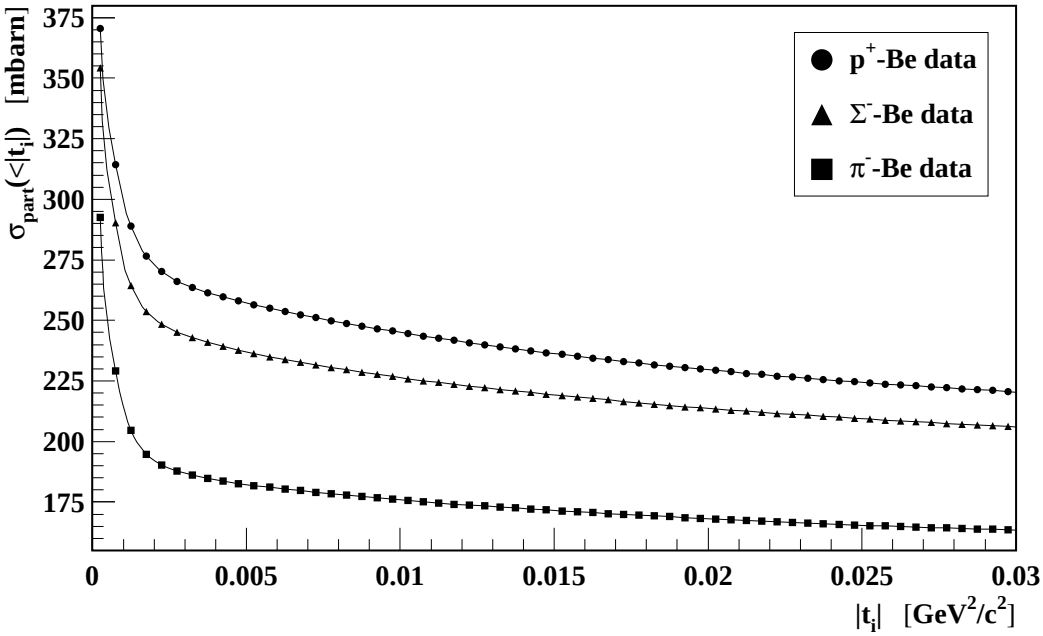

Fig. 3. Spectra of uncorrected partial cross sections resulting from beryllium target data sets.

to equation (4).

Figure 3 shows some spectra for uncorrected partial cross sections. The strong rise of $\sigma_{\mathrm{part}}(< |t_{\mathrm{i}}|)$ for $|t| < 0.002\,\mathrm{GeV}^2/\mathrm{c}^2$ is ascribed to multiple scattering in the target and the finite angular resolution of $\approx 25\,\mu$rad. Differing levels of partial cross-section spectra for beam particles of different kind indicate nicely the dependence of the total cross section on the projectile type.

4.5 Corrections for non-hadronic effects

Partial cross sections were corrected for single Coulomb scattering (C) and for the Coulomb-Nuclear interference effect (CN) evaluating the expression:

$$\sigma_{\mathrm{part}}^{\mathrm{corr}}(<|t_{\mathrm{i}}|) \;=\; \sigma_{\mathrm{part}}(<|t_{\mathrm{i}}|) \;\underbrace{-\int_{-\infty}^{t_{\mathrm{i}}} \left(\frac{d\sigma}{dt'}\right)_{\mathrm{C}} dt'}_{\text{C correction}} \;\underbrace{-\int_{-\infty}^{t_{\mathrm{i}}} \left(\frac{d\sigma}{dt'}\right)_{\mathrm{CN}} dt'}_{\text{CN correction}} \;. \tag{7}$$

Applying the Coulomb correction, a change in the extrapolated cross section of not more than 0.5% is observed for the light targets Be, C and CH_2. For the Cu target a change of up to 11% is noticed. The CN correction is roughly one order of magnitude smaller than the Coulomb correction and has negligible effect on the extrapolated cross section.

4.6 The extrapolation method

As $|t|$ approaches zero, the growth behavior of partial cross sections is governed ideally by the elastic term in equation (6). At small $|t|$, hadronic coherent elastic scattering off nuclei dominates. Thus, we obtain for the elastic term in equation (6), the expression:

$$\int_0^t \left(\frac{d\sigma}{dt'}\right)_{\mathrm{el}}^{\mathrm{hadr}} dt' \;=\; \frac{\sigma_{\mathrm{tot}}^2}{16\pi B_{\mathrm{nuc}}}(1 \;+\; \rho^2)\left[1 \;-\; e^{B_{\mathrm{nuc}}t}\right] \;, \tag{8}$$

where B_{nuc} is the exponential slope observed in hadronic coherent elastic scattering off nuclei. Therefore, we choose the functional form

$$f(\alpha_1, \alpha_2, t) \;=\; \alpha_1\left[1 \;-\; e^{\alpha_2 t}\right] \tag{9}$$

to describe the variation of partial cross sections with respect to $|t_{\mathrm{i}}|$.

The parameters α_1 and α_2 are determined in fitting function (9) to differences in corrected partial cross sections of adjacent t-bins. Thereby, only those corrected partial cross sections where t_{i} is in the range of t_{min} = -0.007 $\mathrm{GeV}^2/\mathrm{c}^2$ to t_{max} = -0.03 $\mathrm{GeV}^2/\mathrm{c}^2$ enter the fit procedure. The limits t_{max} and t_{min} account for experimental sensitivity to hadronic coherent elastic scattering off nuclei. Their derivation is described in section 4.6.1.

Starting from the partial cross section $\sigma_{\mathrm{part}}(<|t_{\mathrm{min}}|)$, the extrapolation to

the total cross section $\sigma_{\rm tot}$ is determined by accounting for the expected growth in partial cross sections from $t_{\rm min}$ to $t = 0$ using the expression:

$$\sigma_{\rm tot} \;=\; \sigma_{\rm part}(<|t_{\rm min}|) \;+\; \alpha_1 \left[1 \;-\; e^{\alpha_2 t_{\rm min}}\right] \;. \tag{10}$$

4.6.1 The limits $t_{\rm min}$ and $t_{\rm max}$ and the sensitivity of the SELEX experiment to coherent hadronic elastic scattering off nuclei

In measurements of hadron-nucleus cross sections, it is essential that the experiment is sensitive to hadronic coherent elastic scattering off nuclei. Further, one must be able to distinguish coherent from incoherent scattering processes off nucleons. In scattering off nuclei, the nucleus can break up when the energy transfer exceeds the binding energy of its nucleons. This leads to a contribution of incoherent scattering off nucleons for $|t| > 0.015$ GeV^2/c^2. In that case, the hadronic differential elastic cross section, entering the elastic term of equation (6), contains two parts:

$$\left(\frac{d\sigma}{dt}\right)^{\rm hadr}_{\rm el} \;=\; \underbrace{\frac{\sigma^2_{\rm tot}({\rm hA})}{16\pi}(1 \;+\; \rho'^2)e^{B_{\rm nuc}t}}_{\text{coherent scattering}} \;+\; \underbrace{{\rm N(A)}\frac{\sigma^2_{\rm tot}({\rm hN})}{16\pi}{\rm e}^{{\rm B_N t}}}_{\text{incoherent scattering}} \;. \tag{11}$$

There is a term for coherent elastic scattering off the nucleus, in which $\sigma_{\rm tot}$(hA) is the total nuclear cross section, and a term for incoherent scattering off nucleons, in which $\sigma_{\rm tot}$(hN) is the corresponding hadron-nucleon cross section. $B_{\rm N}$ is the slope parameter for scattering off nucleons, and N(A) is a factor describing the effective number of nucleons taking part in the incoherent process for target nuclei of mass A (see [5]).

The contribution of the incoherent term decreases the growth behavior of the elastic term in (6) because $B_{\rm N}$ is typically one or more orders of magnitude smaller than $B_{\rm nuc}$. An extrapolation based on partial cross sections, selected in a $|t|$-range far above $0.015\,{\rm GeV}^2/{\rm c}^2$ would lead to a systematically lowered cross-section result as a fraction of the elastic processes is not discriminated. Consequently, we looked for a t-interval $[t_{\rm min};\, t_{\rm max}]$ to select partial cross sections where their growth is dominated by $B_{\rm nuc}$.

The sensitivity of the SELEX spectrometer to hadronic coherent elastic scattering off nuclei was verified by looking at background subtracted but not acceptance corrected differential scattering spectra, which are defined by:

$$\mathrm{S(t)} \;=\; \frac{1}{\rho L \Gamma}\left[\frac{\mathrm{F(t)}}{\mathrm{F_o}} \;-\; \frac{\mathrm{E(t)}}{\mathrm{E_o}}\right] \;. \tag{12}$$

Here, Γ is the width of the t-bins. F(t) (E(t)) is the number of scattering events found in the full-target (empty-target) data sets that fall into the in-

terval $[|t| - \Gamma/2\ ;\ |t| + \Gamma/2]$.

Figure 4 shows a typical example of an S(t) spectrum obtained for Σ^- scattering off carbon nuclei. The spectrum shows three regions governed by apparently different exponential slopes, which can be explained by contributions

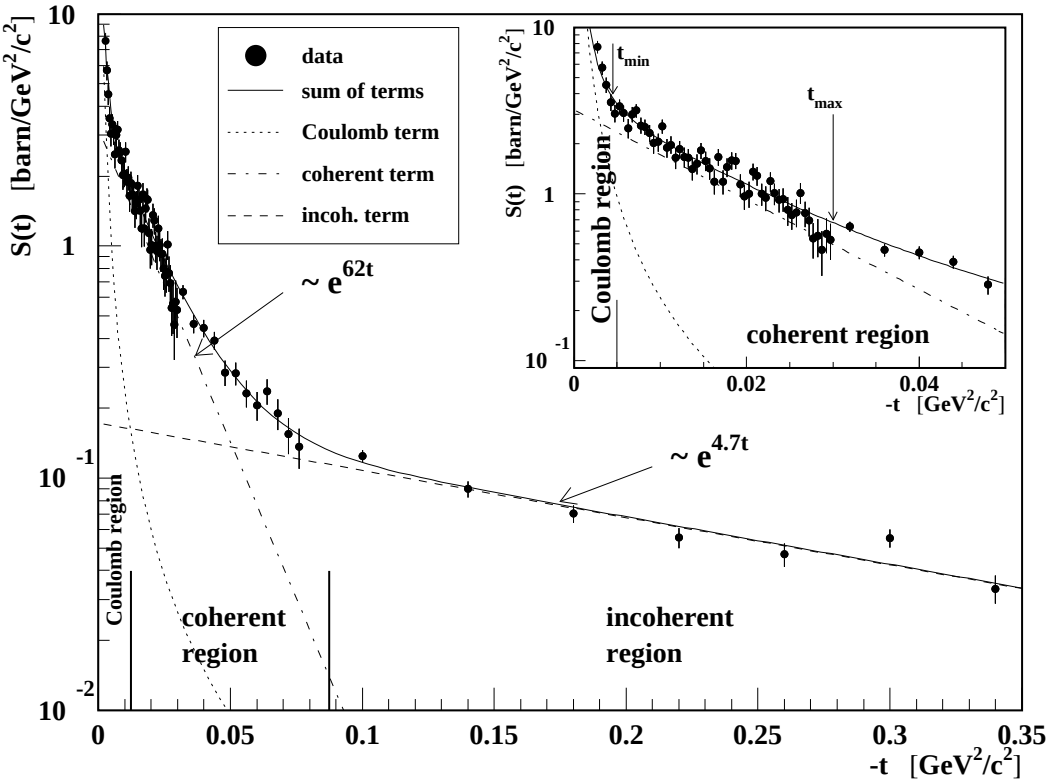

Fig. 4. Differential scattering spectrum obtained for Σ^- carbon reactions, showing the Coulomb, the coherent and the incoherent region.

of Coulomb scattering, coherent elastic scattering and incoherent elastic scattering comparable to measurements described in [5].

Determinations of the slope parameters $B_{\rm nuc}$ and $B_{\rm N}$ in S(t) spectra showed the expected order of magnitude for all targets, and $B_{\rm nuc}$ agreed quite well with data presented in [6]. Furthermore, the magnitude of $B_{\rm nuc}$ is also reflected by the size of parameter α_2 in equation (10), when applying the extrapolation.

From such studies, we choose $t_{\rm max}$ = -0.03 GeV^2/c^2 fixed, as this value is well inside the region dominated by coherent hadronic elastic scattering off nuclei for all targets. The contribution of the integrated incoherent term at this $t_{\rm max}$ is much lower than the integrated coherent term.

Further, to avoid large multiple-scattering corrections, we choose a $t_{\rm min}$ of -0.007 GeV^2/c^2, such that the angular resolution has negligible effect on the extrapolated total cross section.

5 Corrections

5.1 Trigger-rate corrections

The trigger rate influences the reconstruction efficiency for tracks and thus alters the transmission ratios T_{full} and T_{empty} per spill. Figure 5 shows an instructive example of this effect.

Due to the rate effect, our extrapolated total cross-section experiences a shift Δ_{T0} when the average T0-counts, calculated for all empty and all full-target spills separately, differ.

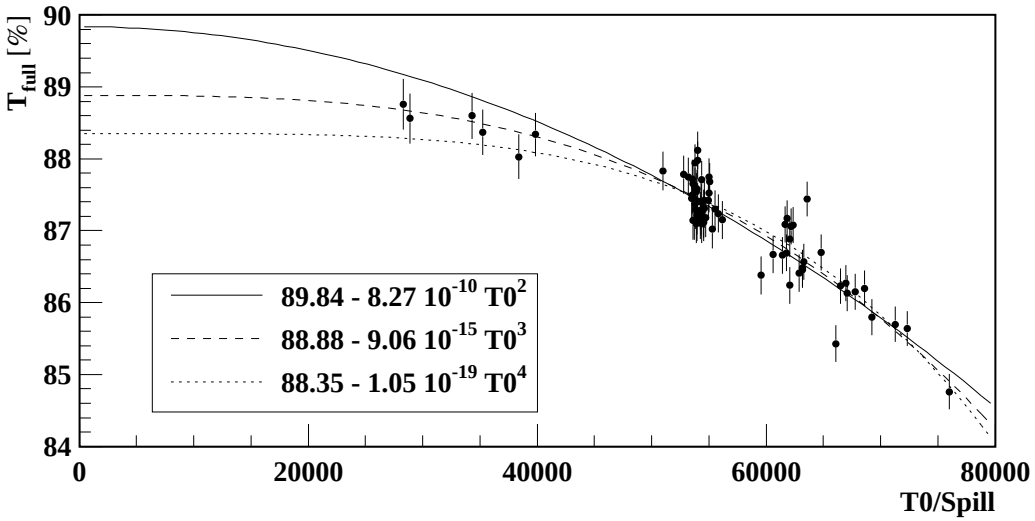

Fig. 5. Dependency of full-target transmission ratios on the T0-count.

To determine the shift Δ_{T0} we calculate full and empty-target transmission ratios per spill for $|t| < 0.01\,\mathrm{GeV}^2/\mathrm{c}^2$ and describe their rate dependency by fitting to the expression

$$\mathrm{T_{fit}(T0)} \;=\; \tilde{\beta}_{1,\mathrm{k}} \;+\; \tilde{\beta}_{2,\mathrm{k}}\mathrm{T0^k}\;. \tag{13}$$

We have studied the effect of different powers (k = 2, 3, 4) to estimate systematic errors.

We choose the average T0-rate $\overline{\mathrm{T0}}$, comprising all full and all empty-target spills as reference rate for the rate correction. Thus, transmission ratios per spill are corrected by evaluating:

$$\underbrace{T^{\mathrm{T0}}_{\mathrm{j,k}}}_{\text{corrected}} \;=\; \underbrace{T_{\mathrm{j}}(|t| < 0.01\mathrm{GeV}^2/\mathrm{c}^2)}_{\text{uncorrected}} \;+\; \underbrace{\tilde{\beta}_{2,\mathrm{k}}(\overline{\mathrm{T0}}^{\mathrm{k}} - \mathrm{T0}^{\mathrm{k}}_{\mathrm{j}})}_{\text{correction}}\;, \tag{14}$$

which results in a set of corrected transmission ratios $T^{T0}_{j,k}$. Fit-function dependent offsets $\Delta_{T0,k}$ are deduced by:

$$\Delta_{T0,k} \;=\; \sigma^{T0,k}_{part}(< 0.01 GeV^2/c^2) \;-\; \sigma_{part}(< 0.01 GeV^2/c^2) \qquad (15)$$

and averaged to a mean offset Δ_{T0}. Total cross sections are then corrected by:

$$\sigma^{T0}_{tot} \;=\; \sigma_{tot} \;+\; \Delta_{T0}\ . \qquad (16)$$

Averaged sizes of the rate correction are presented in table 2. We want to mention that the copper data were taken at higher rate, where the slope of function (13) is steeper. This, together with the small thickness of the copper target, causes large corrections.

5.2 Corrections for beam contaminants

A transition radiation detector does not make an exact particle identification because of statistical fluctuations in X-ray generation and background from various processes. Therefore, when selecting the baryon or the meson component of the hyperon beam by applying cuts on the BTRD plane count, we need to account for:

(1) The amount of meson (baryon) contaminants in the baryon (meson) sample and the effect on the total cross section.
(2) The amount of baryon (meson) contaminants in a specific sample for a measurement with protons or Σ^- (π^-) and the effect on the total cross section.

Once the contaminant fraction ϵ is determined, the experimental cross section σ^{exp}_{tot} can be corrected by the term Δ_{cont} using:

$$\sigma^{(1)}_{tot} \;=\; \sigma^{exp}_{tot} \;+\; \underbrace{\frac{1}{\rho L}\log\left[1 \;+\; \epsilon^{(2)}(e^{-\rho L(\sigma^{(2)}_{tot} \,-\, \sigma^{(1)}_{tot})} \;-\; 1)\right]}_{\text{Correction } \Delta_{cont}}\ . \qquad (17)$$

This formula was derived in [7] for a two component beam having a contamination fraction $\epsilon^{(2)}$.

5.2.1 Beam contaminant determination

In a first step, total cross sections resulting from data sets are corrected for the fraction of mesons (baryons) in a baryon sample (meson sample) us-

ing (17). Therefore, we fit function (1) to normalized BTRD signal spectra, which are recorded for norm tracks. For negative beam these fits yield an average baryon fraction ($\kappa_1 + \kappa_2$) of (47.5 ± 1.6)% and an average meson fraction ($\kappa_3 + \kappa_4$) of (52.5 ± 1.6)%. For positive beam, we measure a baryon fraction of (91.9 ± 1.4)% and a meson fraction of (8.1 ± 1.4)%. To deduce the meson (baryon) contaminant fraction ϵ, we sum the meson (baryon) component of (1) over the TRD plane count region shown in figure 2. Further, the difference $\sigma_{\mathrm{tot}}^{(2)} - \sigma_{\mathrm{tot}}^{(1)}$ is calculated in taking rate corrected extrapolated cross-section results obtained for the meson and the baryon beam component.

In a second step, we account for the main contaminant disturbing a specific measurement for protons, Σ^- and π^-. According to the expected hyperon-beam composition we correct:

(1) For the effect of Ξ^- particles in the baryon sample, when measuring Σ^-A cross sections.
(2) For the effect of Σ^+ particles in the baryon sample, when measuring pA cross sections.
(3) For the effect of K^- particles in the meson sample, when measuring π^-A cross sections.

For case (1), we measure the overall fraction of Ξ^- particles in each negative-beam data sample and for case (2) we measure the overall fraction of Σ^+ particles in each positive-beam data sample. Therefore, we count the decays $\Sigma^- \rightarrow n + \pi^-$, $\Xi^- \rightarrow \Lambda^o + \pi^-$ and $\Sigma^+ \rightarrow n + \pi^+$, reconstructed for a known amount of norm tracks within the field-free region of the M1 magnet. Figure 6 shows some hyperon-mass spectra obtained by the decay reconstruction.

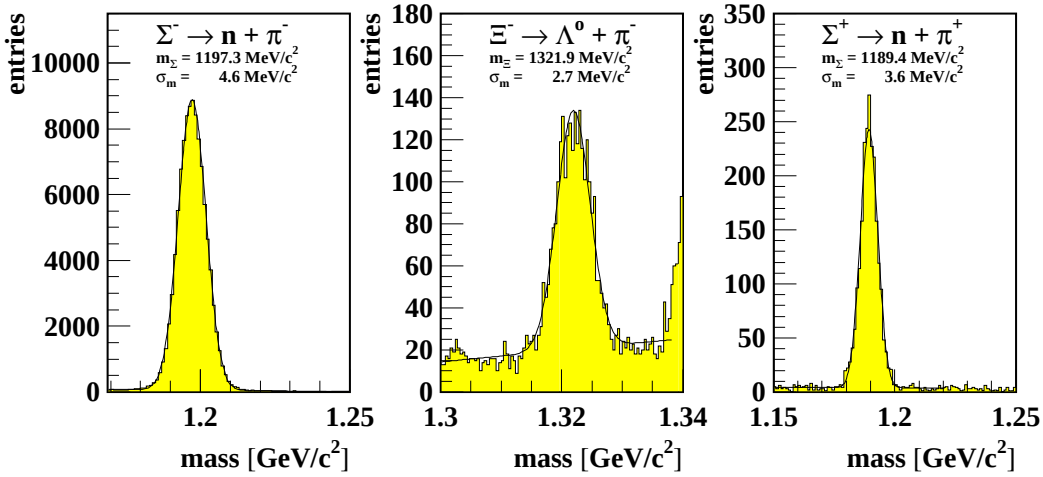

Fig. 6. Hyperon-mass spectra obtained from reconstructed Σ^-, Ξ^- and Σ^+ decays. The spectra are fit to a Gaussian plus a linear background function. m_X is the mean mass found for hyperon X and σ_m is the corresponding mass resolution resulting from the fit.

Particle decay counts are corrected for geometrical acceptance, branching ratio and decay losses after the target, to yield the overall hyperon contaminant fractions. Here, we find an overall Ξ^- fraction of $(1.18 \pm 0.06)\%$, and an overall Σ^+ fraction of $(2.7 \pm 0.7)\%$. These fractions are then divided by the baryon fraction $(\kappa_1 + \kappa_2)$, known from the first step procedure to yield the hyperon contaminant fraction ϵ of the baryon component.

Case (3) requires knowledge of the number of K^- particles in the meson sample. As the SELEX spectrometer does not provide a tool to discriminate 600 GeV/c π^- against K^- particles, we estimate the overall fraction of K^- particles in the sample using particle-flux parameterizations of [1]. This results in an overall K^- fraction of $(1.6 \pm 1.0)\%$, which divided by the meson fraction $(\kappa_3 + \kappa_4)$ yields the K^- contaminant fraction of the meson component.

Calculating the contaminant correction using equation (17) requires knowledge of the total cross sections $\sigma_{\rm tot}(\Xi^-{\rm A})$, $\sigma_{\rm tot}(\Sigma^+{\rm A})$ and $\sigma_{\rm tot}({\rm K}^-{\rm A})$. As data on these cross sections are either scarce or do not exist, we estimate them using approximations like:

$$\sigma_{\rm tot}(\Xi^-{\rm A}) \;\approx\; \sigma_{\rm tot}(\Xi^-{\rm p})\frac{\sigma_{\rm tot}({\rm pA})}{\sigma_{\rm tot}({\rm pp})} \;, \tag{18}$$

and neglect weak but existing energy dependencies. Necessary data for hadron-nucleon cross sections are taken from [4,8] and data for pA-cross sections are taken from [9].

Averaged sizes of the contaminant correction including both correction steps are shown in table 2.

6 Results for hadron-nucleus cross sections

Total cross sections as well as their statistical and systematic errors were determined for each dataset separately. In order to calculate average total cross sections and average systematic errors, we use weighted means. We present the error contributions, the data averaging method and the final results.

6.1 Measurement errors

6.1.1 The statistical error

The dominant error contribution is the statistical error, which is governed by the statistical uncertainty of the partial cross section $\sigma_{\rm part}(< |t_{\rm min}|)$, used in the extrapolation. Further statistical error contributions, originating in other

terms of the error propagated formula (10), are negligible. The statistical errors for each measurement are presented in table 3.

6.1.2 Systematic errors

In this section we briefly describe the systematic errors found during the data analysis. Table 2 gives an overview of the average sizes of these errors as well as the rate correction and the contaminant correction.

Systematic error of the extrapolation δ^{extr}

A significant error contribution is the systematic error in the extrapolation of partial cross sections. This error takes into account the RMS-spread (root mean square) in the extrapolated total cross sections with respect to the extrapolated total cross section at $t_{\mathrm{min}} = -0.007\,\mathrm{GeV}^2/\mathrm{c}^2$, when t_{min} is varied from $-0.004\,\mathrm{GeV}^2/\mathrm{c}^2$ to $-0.01\,\mathrm{GeV}^2/\mathrm{c}^2$.

Cut on the BTRD signal spectrum δ^{BTRD}

Although contaminant and rate corrections are applied for each specific cut on the BTRD signal spectrum, we still observe a variation of the cross section when varying the cut on the TRD plane count by $\pm$ 1 unit around its nominal value. Therefore, we calculate a systematic error, which is the maximum spread in the cross sections found in the cut variation.

Spill to spill fluctuations δ^{fluc}

Here, we compare the statistical error in $\sigma_{\mathrm{part}}(< 0.01\,\mathrm{GeV}^2/\mathrm{c}^2)$, which we calculate by (5) with the error in $\sigma_{\mathrm{part}}(< 0.01\,\mathrm{GeV}^2/\mathrm{c}^2)$ calculated from the experimentally observed RMS-spread of rate corrected transmission ratios per spill. The difference in these errors accounts for remaining non statistical spill to spill fluctuations.

Systematic error of the rate correction δ^{rate}

This error takes into account the error arising from different functional attempts to describe the rate effect presented in section 5.1. Its value is given by the maximum spread of the $\Delta_{\mathrm{T0,k}}$ with respect to their average value Δ_{T0}.

Systematic error of the contaminant correction δ^{cont}

This systematic error accounts for the uncertainty in the fit parameters of the four-fold binomial distribution (1) and for the uncertainty in the contaminant fractions for Σ^+, Ξ^- and K^-.

Uncertainty of the target density δ^{tgt}

The target densities were measured several times, using a pycnometer and

a buoyancy method. Laboratory studies showed systematic discrepancies in the density measurement, which are included in the density errors shown in table 1. These errors are propagated to an error contribution to the total cross sections, which are on a 0.1% level.

		Systematic errors						Corrections	
cross section	p_{lab} [GeV/c]	δ^{extr} [mb]	δ^{BTRD} [mb]	δ^{fluc} [mb]	δ^{rate} [mb]	δ^{cont} [mb]	δ^{tgt} [mb]	Δ_{T0} [mb]	Δ_{cont} [mb]
σ_{tot}(pBe)	536	0.91	0.70	0.25	0.35	0.06	0.30	-1.24	0.62
$\sigma_{tot}(\Sigma^-\mathrm{Be})$	638	1.20	0.49	0.04	0.10	0.07	0.27	-0.93	0.65
$\sigma_{tot}(\pi^-\mathrm{Be})$	638	0.50	0.17	0.22	0.05	0.61	0.21	-0.79	1.00
σ_{tot}(pC)	457	0.90	2.11	0.54	0.38	0.09	0.47	11.22	0.91
σ_{tot}(pC)	490	1.81	1.53	0.68	1.15	0.10	0.47	-3.87	0.86
$\sigma_{tot}(\Sigma^-\mathrm{C})$	598	1.57	1.92	1.21	1.18	0.13	0.43	-6.42	1.12
$\sigma_{tot}(\pi^-\mathrm{C})$	591	1.30	1.40	1.50	0.95	0.63	0.33	-3.11	1.03
$\sigma_{tot}(\Sigma^-\mathrm{CH_2})$	589	2.10	2.55	0.69	0.16	0.16	0.30	3.67	1.44
$\sigma_{tot}(\pi^-\mathrm{CH_2})$	585	1.26	0.96	0.54	0.12	0.75	0.23	2.90	1.21
$\sigma_{tot}(\Sigma^-\mathrm{Cu})$	609	163	41	76	41	0.33	1.23	-754	3.1
$\sigma_{tot}(\pi^-\mathrm{Cu})$	608	85	52	78	36	2.99	1.03	-649	4.7

Table 2
Average sizes of systematic errors and corrections. For explanation of symbols see text of sections 5.1, 5.2 and 6.1.

6.2 Data-averaging and results on hadron-nucleus cross sections

6.2.1 The average total cross section

Total cross-section results $\sigma_{tot,i}$, obtained from i = 1, ..., N data sets, are combined to an average total cross section $\overline{\sigma}_{tot}$ with a statistical error $\delta^{stat}\overline{\sigma}_{tot}$ and an average systematic error $\delta^{syst}\overline{\sigma}_{tot}$. The results are shown in table 3.

We average the total cross-sections $\sigma_{tot,i}$ that correspond to a specific measurement using the weighted mean:

$$\overline{\sigma}_{tot} = \frac{\sum_{i=1}^{N} \omega_i \, \sigma_{tot,i}}{\sum_{i=1}^{N} \omega_i} \quad , \quad \omega_i = \frac{1}{(\delta_i^{stat})^2 + \sum_{j=1}^{M} (\delta_{j,i}^{syst})^2} \, . \tag{19}$$

The weight ω_i includes the statistical error (δ_i^{stat}) of data set i and all j = 1, ..., M systematic errors $\delta_{j,i}^{syst}$ described in section 6.1.1 and 6.1.2.
As the statistical error is supposed to decrease, when adding more data to the

evaluation, we calculate the statistical error in the averaged total cross section by:

$$\delta^{\rm stat}\overline{\sigma}_{\rm tot} \;=\; \sqrt{1/\sum_{\rm i=1}^{\rm N}\frac{1}{(\delta_{\rm i}^{\rm stat})^2}}\;. \tag{20}$$

In assigning a systematic error to an average total cross section $\overline{\sigma}_{\rm tot}$ we assume that the systematic errors of the single measurements can be just averaged. Therefore, we quote as average systematic error:

$$\delta^{\rm syst}\overline{\sigma}_{\rm tot} \;=\; \sqrt{\frac{\sum\limits_{\rm i=1}^{\rm N}\omega_{\rm i}\left[\sum\limits_{\rm j=1}^{\rm M}(\delta_{\rm j,i}^{\rm syst})^2\right]}{\sum\limits_{\rm i=1}^{\rm N}\omega_{\rm i}}}\;, \tag{21}$$

which accounts for the weights $\omega_{\rm i}$ used in (19).

Further, we quote a total error $\delta^{\rm tot}\overline{\sigma}_{\rm tot}$ of the average total cross section, which is calculated from:

$$\delta^{\rm tot}\overline{\sigma}_{\rm tot} \;=\; \sqrt{\left(\delta^{\rm stat}\overline{\sigma}_{\rm tot}\right)^2 \;+\; \left(\delta^{\rm syst}\overline{\sigma}_{\rm tot}\right)^2}\;. \tag{22}$$

cross section	$p_{\rm lab}$ [GeV/c]	$\overline{\sigma}_{\rm tot}$ [mb]	$\delta^{\rm stat}\overline{\sigma}_{\rm tot}$ [mb]	$\delta^{\rm syst}\overline{\sigma}_{\rm tot}$ [mb]	$\delta^{\rm tot}\overline{\sigma}_{\rm tot}$ [mb]
$\sigma_{\rm tot}$(pBe)	536	268.6	± 0.7	± 1.3	± 1.5
$\sigma_{\rm tot}(\Sigma^-{\rm Be})$	638	249.1	± 0.9	± 1.3	± 1.6
$\sigma_{\rm tot}(\pi^-{\rm Be})$	638	188.7	± 0.8	± 0.9	± 1.2
$\sigma_{\rm tot}$(pC)	457	333.6	± 3.1	± 2.4	± 3.9
$\sigma_{\rm tot}$(pC)	490	335.4	± 3.6	± 2.9	± 4.6
$\sigma_{\rm tot}(\Sigma^-{\rm C})$	598	308.9	± 2.1	± 3.8	± 4.3
$\sigma_{\rm tot}(\pi^-{\rm C})$	591	234.1	± 1.5	± 3.1	± 3.5
$\sigma_{\rm tot}(\Sigma^-{\rm CH_2})$	589	376.4	± 2.0	± 4.1	± 4.5
$\sigma_{\rm tot}(\pi^-{\rm CH_2})$	585	286.1	± 1.3	± 2.0	± 2.4
$\sigma_{\rm tot}(\Sigma^-{\rm Cu})$	609	1232	± 133	± 192	± 233
$\sigma_{\rm tot}(\pi^-{\rm Cu})$	608	1032	± 77	± 162	± 179

Table 3
Results for nuclear total cross sections. For explanation of symbols see text of section 6.2.

6.3 Comparison to existing data on hadron-nucleus total cross sections

A literature survey showed that experimental data on hadron-nucleus total cross sections for charged projectiles at high energies is extremely scarce. Information for proton-nucleus and π^--nucleus total cross sections is only provided by the references [5,6,9] and displayed together with our results in the figures 11, 7, 8, 9 and 10. No data were found for Σ^--nucleus total cross sections.

6.3.1 Comparison of nucleon-nucleus total cross sections

In the figures 7 and 8 we display a compilation of proton-nucleus and neutron-nucleus cross sections extracted from [7,10–12] together with our results. As can be seen, the proton-nucleus cross sections of [5] at $p_{lab} = 20\,\mathrm{GeV/c}$ and the neutron-nucleus cross sections are close by. For this reason we assume

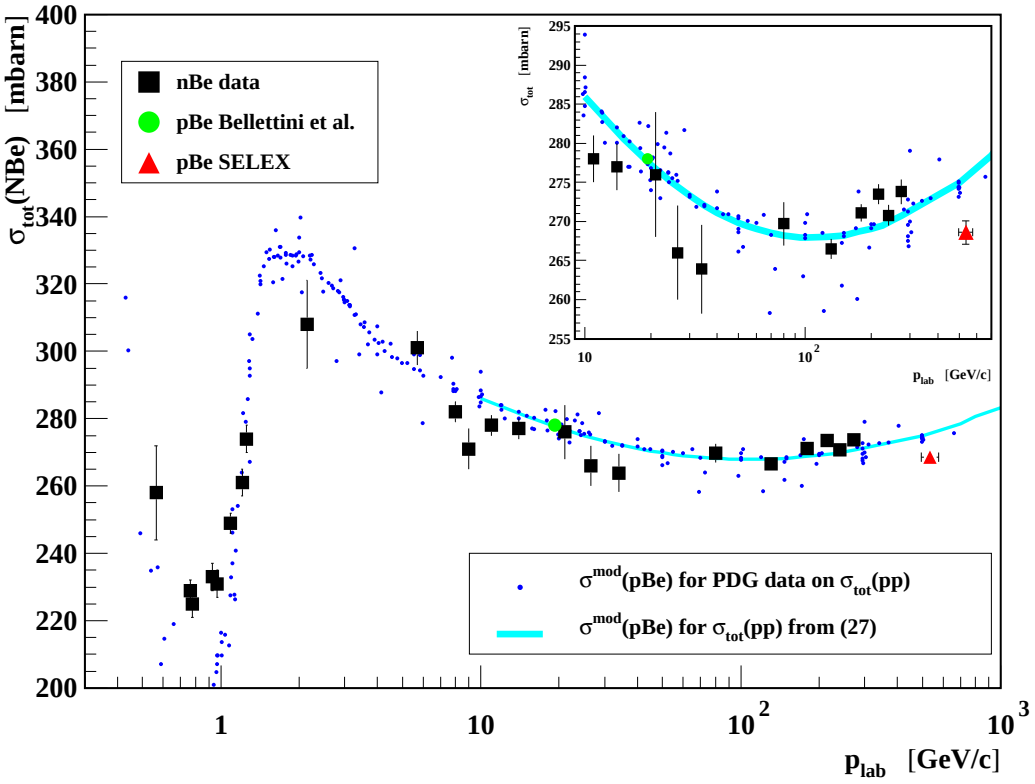

Fig. 7. Summary of experiment data on σ_{tot}(nBe) from [7,10–12] and on σ_{tot}(pBe) from [5] and SELEX. Overlaid are results from the model calculation (see section 7).

that differences between neutron-nucleus and proton-nucleus cross sections are negligibly small above 20 GeV/c. This allows a comparison of our proton-nucleus cross sections with corresponding neutron-nucleus cross-section data available at much higher energy.

Comparing our results with neutron-nucleus cross sections at 131 – 273 GeV/c (data of [7]) shows that our measurements join the sequence of these data points. Averaging the neutron-beryllium total cross sections in this momentum

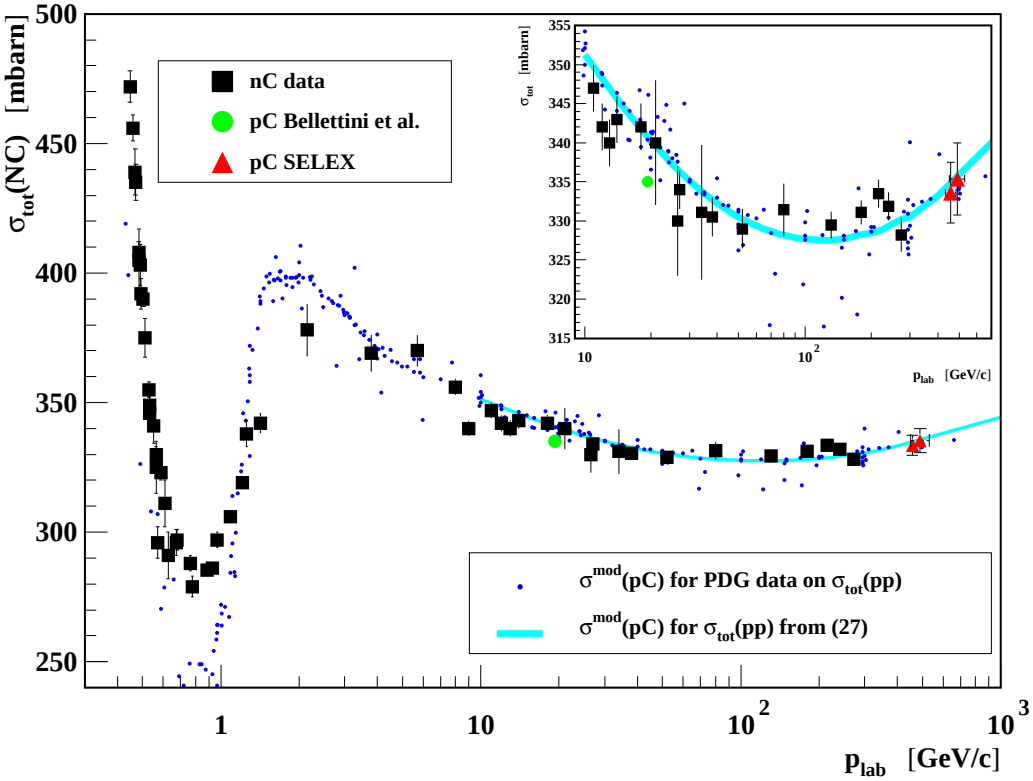

Fig. 8. Summary of experiment data on $\sigma_{\rm tot}$(nC) from [7,10–12] and on $\sigma_{\rm tot}$(pC) from [5] and SELEX. Overlaid are results from the model calculation (see section 7).

range results in 271.0 ± 0.6 mbarn, which is close to our proton-beryllium cross section at 536 GeV/c of 268.6 ± 1.5 mbarn. A similar calculation for the neutron-carbon cross section gives a mean value of 331.0 ± 0.8 mbarn, which is close to our measurements of the proton-carbon cross section around 457 GeV/c of 333.6 ± 3.9 mbarn.

6.4 Comparison of π^--nucleus total cross sections

High-energy data for $\sigma_{\rm tot}(\pi^-{\rm Be})$, $\sigma_{\rm tot}(\pi^-{\rm C})$ and $\sigma_{\rm tot}(\pi^-{\rm Cu})$ that were determined using a transmission technique are presented in the thesis of A. Schiz [9]. Unfortunately, the statistical errors quoted for the π^-A total cross-sections are too large and miss further corrections. Therefore, we present in figure 11, 9 and 10 "normalization factors" for π^--nucleus scattering taken from [6]. These factors are based on the thesis [9], have the meaning of a total π^--nucleus cross section, but result from fits to π^--nucleus elastic scattering data, and have smaller error.

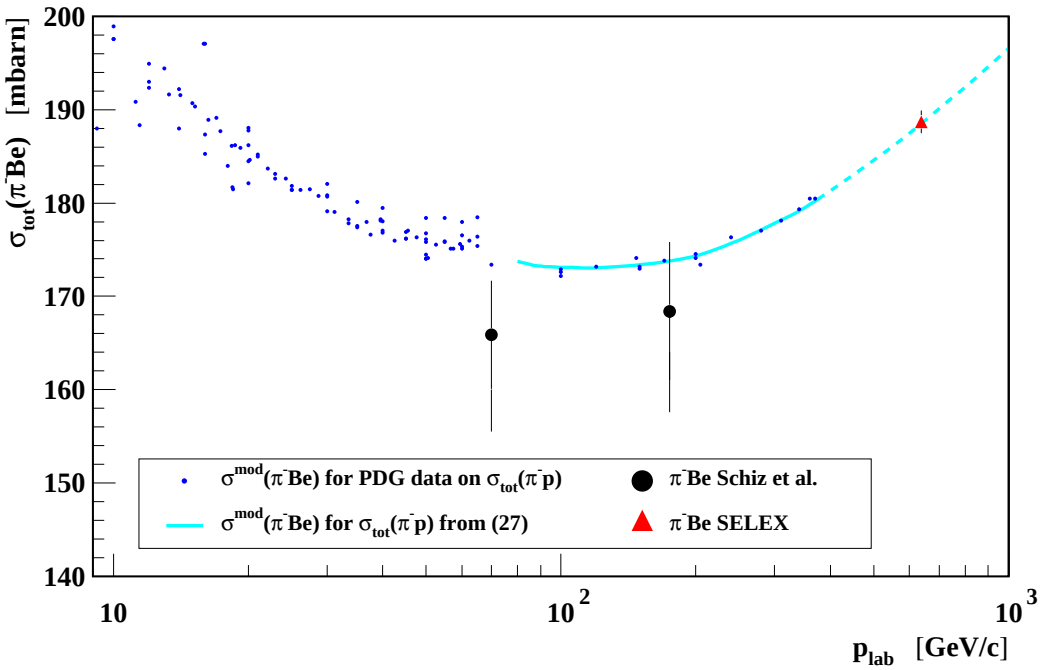

Fig. 9. Summary of experiment data on $\sigma_{\rm tot}(\pi^-{\rm Be})$ from [6] and SELEX. Overlaid are results from the model calculation (see section 7).

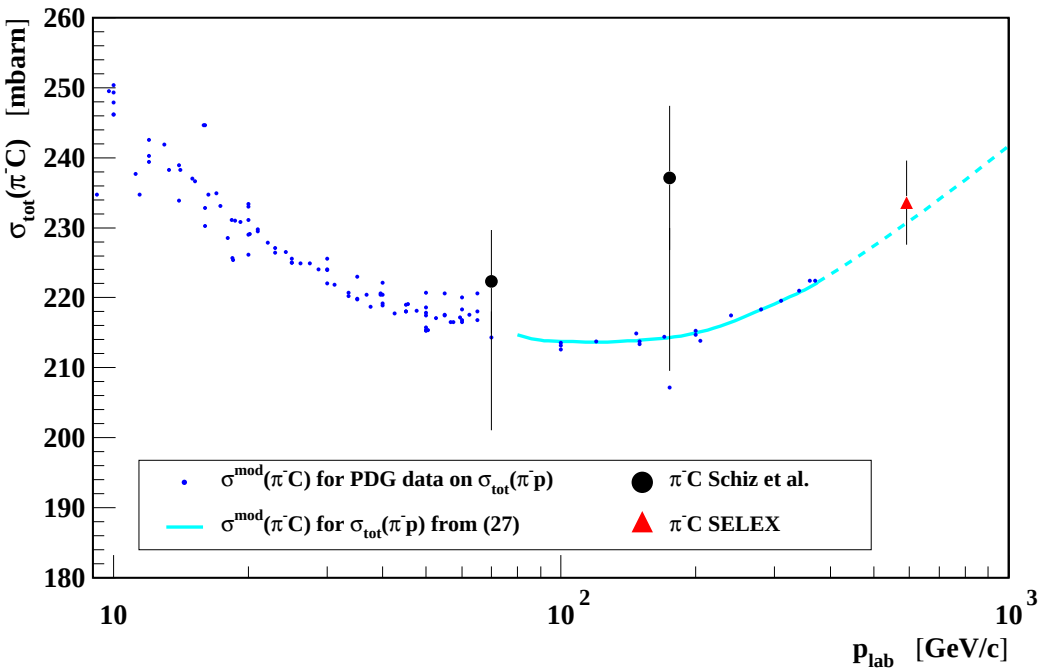

Fig. 10. Summary of experiment data on $\sigma_{\rm tot}(\pi^-{\rm C})$ from [6] and SELEX. Overlaid are results from the model calculation (see section 7).

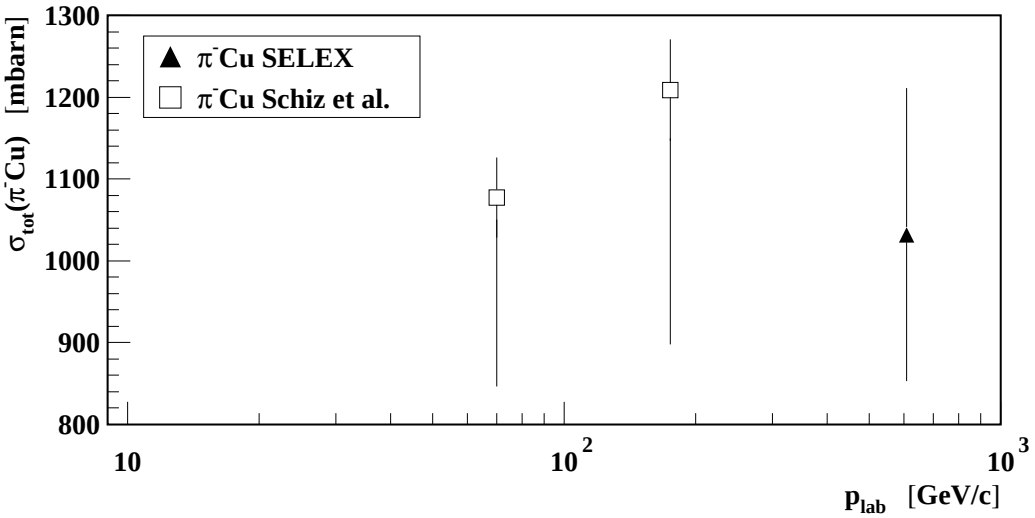

Fig. 11. Results for $\sigma_{\rm tot}(\pi^-{\rm Cu})$ from [6] and SELEX.

The figures 9, 10 and 11 show that the SELEX results for π^-Be, π^-C and π^-Cu cross sections join the displayed normalization factors. However, further and more precise data would allow a more detailed comparison.

7 Model description of hadron-nucleus cross sections

In this section, we introduce a model calculation for hadron-nucleus cross sections and show how well it describes the data.

7.0.1 The Glauber model and the inelastic screening correction

As shown in [7], the Glauber model [13,14] including an inelastic screening correction [15], is very precise in describing neutron-nucleus cross sections at high energy. The Glauber model accounts for the elastic screening effect in nuclei via multiple elastic scattering between the incident hadron h and the nucleons N. As mentioned in [7], nuclear total cross sections calculated by the Glauber model exceed experimental data. This is compensated by taking into account the inelastic screening correction described in [15]. It accounts for inelastic reactions $h + N \to N + X$, which produce an inelastic screening effect. Consequently, a model cross section $\sigma_{\rm tot}^{\rm mod}$ comprises two parts:

$$\sigma_{\rm tot}^{\rm mod}({\rm A}, \sigma_{\rm tot}({\rm hN})) \;=\; \sigma_{\rm tot}^{\rm Gla}({\rm A}, \sigma_{\rm tot}({\rm hN})) \;-\; \Delta\sigma^{\rm Kar}\;. \qquad (23)$$

These are a Glauber model cross section $\sigma_{\rm tot}^{\rm Gla}({\rm A}, \sigma_{\rm tot}({\rm hN}))$ and an inelastic screening correction $\Delta\sigma^{\rm Kar}$.

The Glauber model cross section

According to [14], $\sigma_{\rm tot}^{\rm Gla}({\rm A},\sigma_{\rm tot}({\rm hN}))$ can be calculated by:

$$\sigma_{\rm tot}^{\rm Gla}({\rm hA}) = 4\pi\Re e\left\{\int_0^\infty 1 \;-\; \left[1 \;-\; \frac{(1-i\rho'_{\rm hN})}{2}\sigma_{\rm tot}({\rm hN}){\rm T(b)}\right]^{\rm A} {\rm bdb}\right\} \tag{24}$$

$$ {\rm T(b)} = \frac{1}{2\pi}\int_{\rm o}^\infty {\rm J_o(qb)e^{-B_{hN}\frac{q^2}{2}}S(q)qdq} \quad , \quad {\rm S(q)} \;=\; \frac{4\pi}{\rm q}\int_{\rm o}^\infty {\rm r\sin(qr)\tilde{\rho}(r)dr}\;.$$

Here $\rho'_{\rm hN}$ is the real to the imaginary part of the elastic scattering amplitude in the forward direction observed in hadron-nucleon elastic scattering and b is the impact parameter. $B_{\rm hN}$ is the hadronic slope in hadron-nucleon elastic scattering and $\rm J_o$ is a Bessel function of 0'th order. The nuclear density $\tilde{\rho}(\rm r)$ is normalized as:

$$4\pi\int_0^\infty \tilde{\rho}({\rm r})\,{\rm r^2 dr} \;=\; 1\;. \tag{25}$$

The inelastic screening correction

The inelastic screening correction $\Delta\sigma^{Kar}$, originally formulated in [15] for proton-nucleus reactions, is generalized by:

$$\Delta\sigma^{\rm Kar} = 4\pi\int_{\rm o}^\infty\int_{({\rm m_p}+{\rm m}_\pi)^2}^{(\sqrt{\rm s}-{\rm m_p})^2}\left(\frac{{\rm d^2\sigma}}{{\rm dtdM^2}}\right)_{\rm t=0} {\rm e}^{-\frac{1}{2}\sigma_{\rm tot}({\rm hN}){\rm A}\tilde{\rm T}({\rm b})}\left|{\rm F}(q_{\rm L},\vec{\rm b})\right|^2 {\rm dM^2 d^2 b} \tag{26}$$

$$\tilde{\rm T}(\vec{\rm b}) = \int_{-\infty}^{+\infty}\tilde{\rho}(\vec{\rm b},{\rm z}){\rm dz} \quad , \quad {\rm F}(q_{\rm L},{\rm b}) \;=\; {\rm A}\int_{-\infty}^{+\infty}\tilde{\rho}({\rm b},{\rm z}){\rm e}^{{\rm i}q_{\rm L}{\rm z}}{\rm dz}$$

$$q_{\rm L} = ({\rm M^2} \;-\; {\rm m_p^2})\frac{\rm m_p}{\rm s}\quad .$$

Here $\rm m_p$ is the proton mass and $\rm m_\pi$ is the pion mass. The double differential cross section $\rm d^2\sigma/dtdM^2$ describes the inelastic reaction $h + N \to N + X$ of the incident hadron h with a nucleon N, where the resulting final state X has an invariant mass squared of $\rm M^2$.

7.0.2 Input parameters for the total cross-section model

Model input parameters are $\sigma_{\rm tot}(\rm hN)$, $\rho'_{\rm hN}$, $B_{\rm hN}$, $\tilde{\rho}(\rm r)$ and $({\rm d^2\sigma/dtdM^2})|_{\rm t=0}$. All of them are extracted from experimental data with $N = \rm p$.

Input parameter $\sigma_{\rm tot}$(hN)

To be able to access $\sigma_{\rm tot}$(hN) for special ranges of center of mass energies $\sqrt{\rm s}$, data on pp and π^-p total cross sections, taken from [8], were fit to a smooth function:

$$\sigma_{\rm tot}({\rm hp,s}) \;=\; \frac{{\rm a_o}}{{\rm s}^{\rm a_1}} \;+\; {\rm a_2}\log^2({\rm s})\;. \tag{27}$$

The fit-parameters $a_{\rm i}$, their errors and the validity range of each parameterization, are shown in table 4. The result of each parameterization is in mbarn, when using s in GeV^2.

reaction	a_o	a_1	a_2	momentum range
pp	49.51 ± 0.26	0.097 ± 0.002	0.314 ± 0.004	10 ... 3000 GeV/c
π^-p	55.2 ± 7.2	0.255 ± 0.032	0.346 ± 0.020	80 ... 380 GeV/c

Table 4
Fit-Parameters and validity range of the total cross-section parameterizations.

Input parameter $\rho'_{\rm hp}$

We parameterize $\rho'_{\rm pp}({\rm p_{lab}})$ and $\rho'_{\pi^-{\rm p}}({\rm p_{lab}})$, using data on $\rho'_{\rm pp}$ from [16–28] and data on $\rho'_{\pi^-{\rm p}}$ from [16,21,29,30], assuming that ρ' reaches a constant value

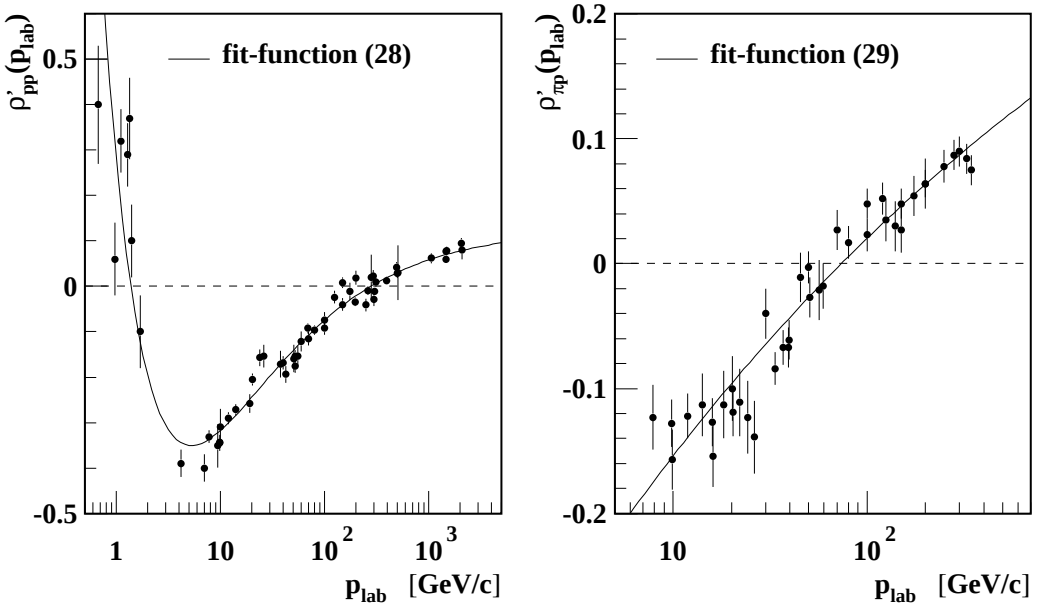

Fig. 12. Our parameterizations for $\rho'_{\rm pp}({\rm p_{lab}})$ and $\rho'_{\pi^-{\rm p}}({\rm p_{lab}})$ together with experimental data from [16–28].

when p_{lab} goes to infinity. Our fits are

$$\rho'_{pp}(p_{lab}) = +\frac{6.8}{p_{lab}^{0.742}} - \frac{6.6}{p_{lab}^{0.599}} + 0.124 \quad \text{for } 0.8 \text{ GeV/c} < p_{lab} < 2100 \text{ GeV/c} \tag{28}$$

$$\rho'_{\pi^- p}(p_{lab}) = -\frac{0.92}{p_{lab}^{0.54}} + 0.54 \quad \text{for } 8.0 \text{ GeV/c} < p_{lab} < 345 \text{ GeV/c} , \tag{29}$$

where p_{lab} is in GeV/c. Figure 12 displays these fit-functions together with all data points included in the fit.

Input parameter B_{hp}

For the hadronic slope parameters B_{pp} and $B_{\pi^- p}$ we take the parameterizations presented in [31]:

$$B_{pp}(p_{lab}) = \begin{cases} B_{pp,1} = 11.13 - \frac{6.21}{\sqrt{p_{lab}}} + 0.30 \log\{p_{lab}\} & ; \quad q^2 = 0.02 \\ B_{pp,2} = 9.26 - \frac{4.94}{\sqrt{p_{lab}}} + 0.28 \log\{p_{lab}\} & ; \quad q^2 = 0.20 \\ B_{pp,3} = 9.67 - \frac{7.51}{\sqrt{p_{lab}}} + 0.10 \log\{p_{lab}\} & ; \quad q^2 = 0.40 \end{cases} \tag{30}$$

$$B_{\pi p}(p_{lab}) = \begin{cases} B_{\pi p,1} = 9.11 + \frac{0.65}{\sqrt{p_{lab}}} + 0.29 \log\{p_{lab}\} & ; \quad q^2 = 0.02 \\ B_{\pi p,2} = 6.95 + \frac{0.65}{\sqrt{p_{lab}}} + 0.27 \log\{p_{lab}\} & ; \quad q^2 = 0.20 \\ B_{\pi p,3} = 6.13 + \frac{0.65}{\sqrt{p_{lab}}} + 0.25 \log\{p_{lab}\} & ; \quad q^2 = 0.40 . \end{cases} \tag{31}$$

Here, q^2 is in units of GeV$^2/c^2$. These parameterizations are linearly interpolated to account for the dependency of B_{hN} on both p_{lab} and q^2.

Input parameter $(d^2\sigma/dtdM^2)|_{t=0}$

To calculate the inelastic screening correction $\Delta\sigma^{Kar}$, we use the parameterization of $(d^2\sigma/dtdM^2)|_{t=0}$ for the process $p + p \to p + X$, given in [7]:

$$\left(\frac{d^2\sigma}{dtdM^2}\right)_{t=0} = \begin{cases} 26.470(M^2 - 1.17) - 35.969(M^2 - 1.17)^2 + \\ 18.470(M^2 - 1.17)^3 - 4.143(M^2 - 1.17)^4 + \\ 0.341(M^2 - 1.17)^5 \quad \text{for } 1.17 < M^2 < 5 \text{ GeV}^2/c^2 \\ \frac{4.4}{M^2} \qquad\qquad\qquad\qquad \text{for } M^2 > 5 \text{ GeV}^2/c^2 \end{cases} . \tag{32}$$

In addition, we also use more recent parameterizations for $(d^2\sigma/dtdM^2)|_{t=0}$ to describe the processes $p + p \to p + X$ and $\pi + p \to p + X$, which are pre-

sented in [32] and are based on calculations of triple-Regge diagrams in [33]. For $M^2 \leq M_o^2$, these parameterizations consist of a background term and a sum of non-energy-dependent resonance terms. In case $M^2 > M_o^2$ the parameterizations consist of a sum over contributions from triple-Regge diagrams:

$$\left(\frac{d^2\sigma}{dtdM^2}\right)_{t=0} = \begin{cases} \sum_i \frac{a_i}{(M^2-M_i^2)^2+\Gamma_i} + \frac{c_f(M^2-M_{min}^2)}{(M^2-M_{min}^2)^2+d_f} & , \; M^2 \leq M_o^2 \\ \sum_k V_k \left(\frac{M^2}{s}\right)^{\alpha_{k(0)}-\beta_{k(0)}-\beta'_{k(0)}} \frac{1}{s^{2-\alpha_{k(0)}}} & , \; M^2 > M_o^2 \end{cases} . \tag{33}$$

Instead of displaying the large amount of parameters for equation (33), which are taken from calculations in [33], we display the parameterizations (32) and (33) in figure 13.

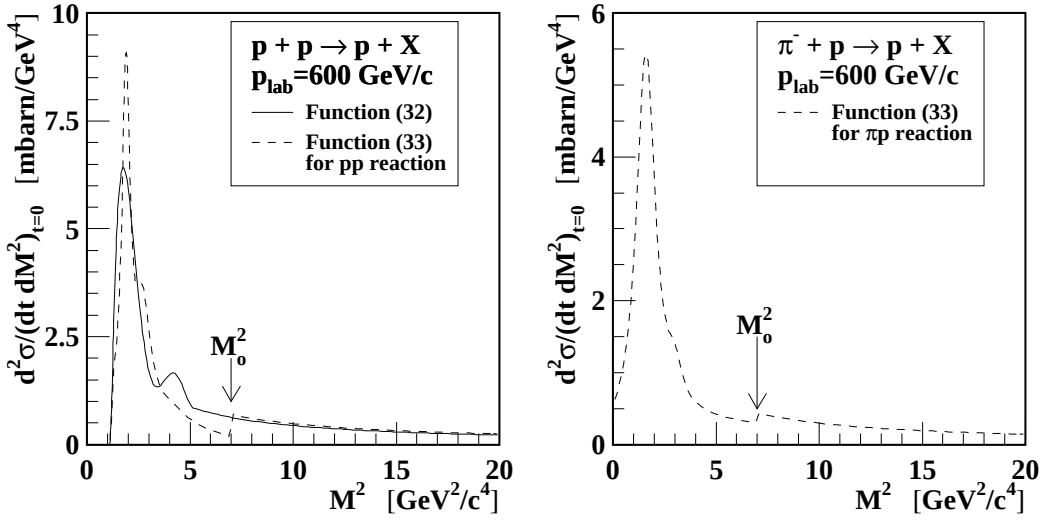

Fig. 13. The parameterizations (32) and (33) evaluated for $p_{lab} = 600\,GeV/c$.

Compared to (33), parameterization (32) has no s-dependence. Further, parameterization (33) is not continuous and the resonance sizes are quite different for $p + p \to p + X$.

Input parameter $\tilde{\rho}(r)$

In the calculations, we use density distributions $\tilde{\rho}(r)$ that are based on the harmonic-oscillator model:

$$\tilde{\rho}(r) = \rho_o \left[1 + \tilde{\alpha}\left(\frac{r}{a_{rad}}\right)^2\right] e^{-\left(\frac{r}{a_{rad}}\right)^2} . \tag{34}$$

This offers the possibility to calculate some integrals in an analytic way and gives a better description of the (charge-) density distribution for light nuclei

than a standard two-parameter Fermi parameterization.

nucleus	data from [34] e-A scattering		fit result using (32) in $\sigma_{tot}^{mod}(NA, a_{rad})$	fit result using (33) in $\sigma_{tot}^{mod}(NA, a_{rad})$
	$\tilde{\alpha}$	a_{rad} [fm]	a_{rad} [fm]	a_{rad} [fm]
beryllium	0.611	1.791	1.89981	2.02914
carbon	1.067	1.687	1.79247	1.89277

Table 5
Parameters of the density distribution $\tilde{\rho}(r)$ from electron-nucleus elastic scattering [34] and the radius parameters resulting from a fit of $\sigma_{tot}^{mod}(a_{rad}, p_{lab})$ to nA cross-section data in the momentum range 10 – 273 GeV/c.

As reported in [7], we also find that the model does not provide a good description of neutron-nucleus total cross sections if one uses both $\tilde{\alpha}$ and a_{rad} from electron-scattering data [34]. Therefore, we used $\tilde{\alpha}$ values from [34] and adjusted the radius parameter a_{rad}, such that the model cross section $\sigma_{tot}^{mod}(NA, a_{rad})$ gives a best description of nA-cross section data in the momentum range 10 – 273 GeV/c. Adjusting of a_{rad} was done for each nucleus and for each of the parameterizations (32) and (33) separately. Table 5 gives a summary of the density parameters.

7.0.3 Results of the model calculations

Results for nucleon-nucleus model cross sections

To show the quality of our model calculation after adjusting the nuclear density parameter a_{rad}, we evaluated the total cross sections $\sigma_{tot}^{mod}(Be, \sigma_{tot}(pp))$ and $\sigma_{tot}^{mod}(C, \sigma_{tot}(pp))$ using function (32). This was done for data on $\sigma_{tot}(pp)$ taken from [8] and for values on $\sigma_{tot}(pp)$ resulting from our fit (27). The calculations were done at many different values of p_{lab} to show the behavior over the entire high momentum region. Scatter in the model calculations (observed when experimental data on $\sigma_{tot}(pp)$ are used) demonstrate the sensitivity of the model to small changes in $\sigma_{tot}(pp)$.

Summaries of calculation and data are shown in figure 7 and 8. They show that the calculations reflect quite well the cross-section data for $p_{lab} > 5$ GeV/c. The nBe data of [7] in the range 131 – 273 GeV/c suggest a rise of the nBe cross section with energy that is also indicated by the model calculation. Our data point does not show any rise for pBe. In the case of nC cross sections our measurements join both data at lower energy and calculation very nicely.

Results for π^--nucleus model cross sections

We evaluated the cross sections $\sigma_{tot}^{mod}(Be, \sigma_{tot}(\pi^- p))$ and $\sigma_{tot}^{mod}(C, \sigma_{tot}(\pi^- p))$ using function (33) and the corresponding nuclear density parameter a_{rad},

which was determined by a fit of the model cross section to neutron-nucleus data. All further input parameters are specific for π^-p-reactions. The calculations were done for data on $\sigma_{\rm tot}(\pi^-{\rm p})$ taken from [8] and for values from function (27).

Results are shown in figure 9 and 10 together with data for π^--nucleus total cross sections from [6] and the SELEX experiment. The figures show that the calculations match our measurements quite well and agree within errors with lower-energy data from [6].

8 Results for hadron-nucleon cross sections

The hadron-nucleon cross sections $\sigma_{\rm tot}(\Sigma^-{\rm N})$ and $\sigma_{\rm tot}(\pi^-{\rm N})$ were first determined by a CH_2 – C method. As this method provides hadron-nucleon cross sections only with a precision on the order of 10%, we improved the precision using a method which takes advantage of the more precise hadron-nucleus cross-section ratios.

8.1 Hadron-nucleon cross sections using a CH_2 – C difference method

The hadron-nucleon cross sections $\sigma_{\rm tot}(\Sigma^-{\rm N})$ and $\sigma_{\rm tot}(\pi^-{\rm N})$ can be deduced from corresponding cross sections measured on carbon and polyethylene by:

$$\sigma_{\rm tot}({\rm hN}) \;=\; \frac{1}{2}\left[\sigma_{\rm tot}({\rm hCH_2}) \;-\; \sigma_{\rm tot}({\rm hC})\right] \;, \tag{35}$$

where h denotes the incident hadron. Results obtained by this method are presented in table 9. The quoted errors are calculated from the total errors in the hadron-nucleus cross sections given in table 3.

8.2 Hadron-nucleon cross sections deduced from hadron-nucleus cross sections

In a second approach, we deduce hadron-nucleon cross sections from ratios of measured hadron-nucleus cross sections. To motivate the method, we first derive empirical relations between hadron-nucleon and hadron-nucleus cross section ratios, which we then refine using the model calculation described in section 7.

To derive empirical relations between hadron-nucleon and hadron-nucleus

cross section ratios we use data on hadron-nucleon cross sections around 137 GeV/c from [4,8], and obtain the hadron-nucleon cross-section ratios:

$$\frac{\sigma_{\rm tot}(\pi^-{\rm p})}{\sigma_{\rm tot}({\rm pp})} \approx 0.635 \pm 0.006, \qquad \frac{\sigma_{\rm tot}(\Sigma^-{\rm p})}{\sigma_{\rm tot}({\rm pp})} \approx 0.901 \pm 0.012\ . \tag{36}$$

Next, we build nuclear cross-section ratios using our measurements for the Σ^-A, π^-A and pA cross sections from table 3.

Our pA cross sections were measured at lower laboratory momentum than the corresponding Σ^-A or π^-A cross sections. To correct for this, we scale the pA cross sections by a factor $k_{\rm scale}$ before building the cross-section ratio. The scale factor takes into account the growth of the pA cross section from the laboratory momentum where it was measured to the larger laboratory momentum of the corresponding Σ^-A or π^-A cross section. Scaling factors are calculated using the model described in section 7. They are displayed together with the nuclear cross-section ratios in table 6.

scaled cross-section ratio	$p_{\rm lab}$ [GeV/c]	$k_{\rm scale}$
$\sigma_{\rm tot}(\pi^-{\rm Be})/\sigma_{\rm tot}({\rm pBe}) = 0.698 \pm 0.006$	640	1.0058
$\sigma_{\rm tot}(\pi^-{\rm C})/\sigma_{\rm tot}({\rm pC}) = 0.695 \pm 0.014$	590	1.0036
$\sigma_{\rm tot}(\Sigma^-{\rm Be})/\sigma_{\rm tot}({\rm pBe}) = 0.922 \pm 0.008$	640	1.0058
$\sigma_{\rm tot}(\Sigma^-{\rm C})/\sigma_{\rm tot}({\rm pC}) = 0.917 \pm 0.018$	590	1.0040

Table 6
Nuclear cross-section ratios. The pA-cross section is scaled by $k_{\rm scale}$ to account for the discrepancy in laboratory momenta of the cross sections used in the ratio.

The nuclear ratios show that the π^-A cross sections are about 0.7 times and the Σ^-A cross sections are about 0.92 times smaller than the pA cross section.

To get a first relation between hadron-nucleon and hadron-nucleus cross sections, we ignore the weak energy dependence of the cross-section ratios. Calculating the ratios of hadron-nucleon to hadron-nucleus cross-section ratios using the above data gives the results presented in table 7.

The double ratios show a small but significant deviation from one especially for ratios involving π^- cross sections. From this empirical observation it follows that a hadron-nucleon cross section $\sigma_{\rm tot}(hN)$ can be approximately derived from the pp cross section and a hadron-nucleus cross-section ratio using the relation:

$$\sigma_{\rm tot}(hN) \approx \kappa \times \sigma_{\rm tot}({\rm pp}) \times \left(\frac{\sigma_{\rm tot}({\rm hA})}{\sigma_{\rm tot}({\rm pA})}\right)\ , \tag{37}$$

double ratio	result	double ratio	result
$\frac{\sigma_{\rm tot}(\Sigma^-{\rm p})/\sigma_{\rm tot}({\rm pp})}{\sigma_{\rm tot}(\Sigma^-{\rm Be})/\sigma_{\rm tot}({\rm pBe})}$	0.977 ± 0.016	$\frac{\sigma_{\rm tot}(\pi^-{\rm p})/\sigma_{\rm tot}({\rm pp})}{\sigma_{\rm tot}(\pi^-{\rm Be})/\sigma_{\rm tot}({\rm pBe})}$	0.910 ± 0.012
$\frac{\sigma_{\rm tot}(\Sigma^-{\rm p})/\sigma_{\rm tot}({\rm pp})}{\sigma_{\rm tot}(\Sigma^-{\rm C})/\sigma_{\rm tot}({\rm pC})}$	0.983 ± 0.023	$\frac{\sigma_{\rm tot}(\pi^-{\rm p})/\sigma_{\rm tot}({\rm pp})}{\sigma_{\rm tot}(\pi^-{\rm C})/\sigma_{\rm tot}({\rm pC})}$	0.915 ± 0.020
average (κ)	0.980 ± 0.014	average (κ)	0.913 ± 0.012

Table 7
Ratios of the hadronic cross-section ratios at 137 GeV/c and the nuclear cross-section ratios around 600 GeV/c.

where κ is a parameter specific for the cross section ratio (compare with table 7). If we set $\kappa = 1$ for simplicity, we see that the precision of (37) is about 10%. The precision is improved by adequate adjusting of κ.

Unfortunately we cannot empirically derive κ from experimental cross sections for laboratory momenta around 600 GeV/c as necessary cross-section data is missing. Thus, as we want to deduce hadron-nucleon cross sections from nuclear cross-section ratios with best precision, we improve the relation between hadron-nucleon and hadron-nucleus cross sections using the total cross-section model that was introduced in section 7.

The idea of the model-based ratio method is the following: Rewriting (37) yields the following relation between the experimental hadron-nucleus and the model based hadron-nucleus cross-section ratios.

$$\underbrace{\frac{\overline{\sigma}_{\rm tot}(hA)}{\overline{\sigma}_{\rm tot}({\rm pA})}}_{\text{experimental}} = \underbrace{\frac{\sigma_{\rm tot}^{\rm mod}({\rm A}, \sigma_{\rm tot}({\rm hN}))}{\sigma_{\rm tot}^{\rm mod}({\rm A}, \sigma_{\rm tot}({\rm pN}))}}_{\text{theory + } \sigma_{\rm tot}\text{-data}} . \tag{38}$$

Taking the ratio of model based quantities reduces the effect of uncertainties in the cross-section model. Further, as data for $\sigma_{\rm tot}({\rm pp})$ is most precise and exists over a large energy range, it is convenient to use proton-nucleus cross sections in the denominator. As the energy dependence of the pp cross section is known at SELEX energies and the model is adjusted to describe NA cross sections for $p_{\rm lab} > 10$ GeV/c, the energy dependence of $\sigma_{\rm tot}({\rm hp})$, which we want to determine, is taken into account through the energy dependence of the pp cross section.

To deduce the cross section $\sigma_{\rm tot}({\rm hN})$ from the measured nuclear cross-section ratio, we fix $\sigma_{\rm tot}({\rm pN})$ $(= \sigma_{\rm tot}({\rm pp}))$ first and calculate the denominator $\sigma_{\rm tot}^{\rm mod}(A, \sigma_{\rm tot}({\rm pp}))$ by taking $\sigma_{\rm tot}({\rm pp})$ from parameterization (27) evaluated at the laboratory momentum of the nuclear cross-section ratio as given in table 6. Iterating with respect to the model input parameter $\sigma_{\rm tot}({\rm hN})$ until the model based total cross-section ratio in (38) equals the experimental one, yields the desired hadron-nucleon cross section. At SELEX energy we interpret the result $\sigma_{\rm tot}({\rm hN})$ identical to $\sigma_{\rm tot}({\rm hp})$.

8.2.1 Results for $\sigma_{\rm tot}(\Sigma^-{\rm N})$ and $\sigma_{\rm tot}(\pi^-{\rm N})$ using the ratio method

Results of the ratio method are presented in table 9 together with the results from the CH_2 – C method. The errors of hadron-nucleon cross sections resulting from the ratio method include both the error in the measured nuclear cross-section ratio and model uncertainties. Model uncertainties are taken into account by adding the error of a model cross-section ratio in quadrature to the error of the corresponding experimental cross-section ratio given in table 6. The error in the model cross-section ratio is derived from the discrepancy between model and measured cross sections observed for pA and π^-A total cross sections. Typical sizes of these discrepancies are shown in table 8.

reaction	measured cross section $\times$ $k_{\rm scale}$ [mbarn]	calculated cross section [mbarn]	cross-section difference [mbarn]	nominal $p_{\rm lab}$ [GeV/c]
$\sigma_{\rm tot}(\pi^-{\rm Be})$	188.7	188.8	0.1	640
$\sigma_{\rm tot}(\pi^-{\rm C})$	234.1	231.4	2.7	590
$\sigma_{\rm tot}({\rm pBe})$	270.2	277.0	6.8	640
$\sigma_{\rm tot}({\rm pC})$	336.8	335.9	0.9	590

Table 8
Discrepancy between model and measured total cross sections. The measured pA cross sections are scaled by $k_{\rm scale}$.

Further, as two different parameterizations for $({\rm d}^2\sigma/{\rm dtdM}^2)|_{\rm t=0}$ are available, we evaluate the ratio method for both, average the results and include their difference in the error of the mean.

Finally, we want to mention that as little data exists for Σ^- scattering, we insert in the computation of $\sigma_{\rm tot}^{\rm mod}(\Sigma^-{\rm A})$ for $B_{\Sigma^-{\rm N}}$, $\rho'_{\Sigma^-{\rm N}}$ and $({\rm d}^2\sigma/{\rm dtdM}^2)|_{\rm t=0}$, the parameterizations from pp-reactions.

method description	$\sigma_{\rm tot}(\Sigma^-{\rm N})$ [mbarn]	$\sigma_{\rm tot}(\pi^-{\rm N})$ [mbarn]	$p_{\rm lab}$ [GeV/c]
difference method	33.7 ± 3.1	26.0 ± 2.1	585
ratio method, Be data	37.4 ± 1.3	27.1 ± 1.5	640
ratio method, C data	37.0 ± 0.8	26.4 ± 1.3	595
total average	37.0 ± 0.7	26.6 ± 0.9	610

Table 9
The total cross sections $\sigma_{\rm tot}(\Sigma^-{\rm N})$ and $\sigma_{\rm tot}(\pi^-{\rm N})$ resulting from all methods and their average.

Comparing the hadron-nucleon cross sections of the ratio and the difference method, we find good agreement of the results with respect to their errors.

As final result, we average the hadron-nucleon cross-section values from all methods. These total averages are presented in the last row of table 9 together with a corresponding averaged laboratory momentum.

8.3 Comparison to models

8.3.1 Comparisons for $\sigma_{\rm tot}(\pi^-{\rm p})$

Most of the models and parameterizations for hadron-nucleon cross sections exploit the interplay of 2 contributions. The Pomeron contribution, which dominates asymptotics at high energies; and the Regge contribution, which is important at low and medium energies. Many models (e.g. [35,36]) describe the energy dependence of total cross sections quite well. Because of this, we simply display in figure 14 experimental data from [8] and SELEX together with the parameterization for $\sigma_{\rm tot}(\pi^-{\rm p,s})$:

$$\sigma_{\rm tot}(\pi^-{\rm p,s}) = 35.9{\rm s}^{-0.45} \; + \; 13.7{\rm s}^{+0.079} \qquad (39)$$
$$\text{for } {\rm p_{lab}} \; > 10\,{\rm GeV/c},\ \sigma_{\rm tot} \text{ in mbarn, s in GeV}^2\ ,$$

which was presented in the particle data book 1996 [37]. We want to mention that in the data files of the particle data group errors in the high precision

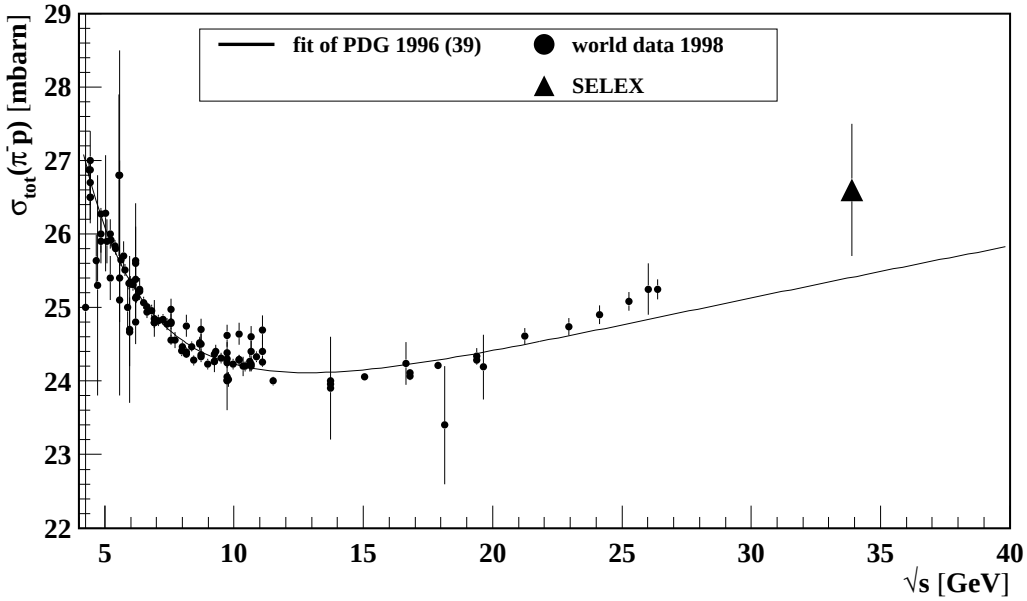

Fig. 14. Existing data for $\sigma_{\rm tot}(\pi^-{\rm p})$ in comparison with our results and parameterization (39) of the particle data group 1996.

data of A.S. Caroll et al. [38] are not completely taken over from the reference. Thus, we added the missing error contributions (systematic error due to target

density and extrapolation uncertainty) in quadrature.

We point out that so far the total cross section $\sigma_{\rm tot}(\pi^-{\rm p})$ has been measured only up to $p_{\rm lab} = 370\,{\rm GeV/c}$ [38]. Thus, the SELEX total average for $\sigma_{\rm tot}(\pi^-{\rm N})$ at 610 GeV/c is the first new measurement at higher laboratory momentum.

In figure 14 parameterization (39) of the Particle Data Group, which uses a Pomeron intercept of 0.079, is overlaid to the data. The qualitative inspection of (39) suggests that it is strongly weighted by the huge amount of low energy data points and does not sufficiently well take into account the very accurate data of [38] at high energy. Our result seems to strengthen the trend observed in data of [38]. This trend implies a faster rise of the π^-p cross section with increasing energy than represented by (39). We just want to point out this observation, which may turn out to be in conflict with the belief that the energy increase of hadronic cross sections is universal. Further, we do not give any quantitative estimate of the Pomeron intercept for the π^-p cross section. Its value is correlated to the assumed Regge contribution at low energy and its determination requires a careful analysis of the data.

8.3.2 Comparisons for $\sigma_{\rm tot}(\Sigma^-{\rm p})$

Up to now, data on the total cross section $\sigma_{\rm tot}(\Sigma^-{\rm p})$ are still scarce. In the past, there have been only two hyperon-beam experiments [4,39] giving information about the behavior of $\sigma_{\rm tot}(\Sigma^-{\rm p})$ in the momentum range 19 –

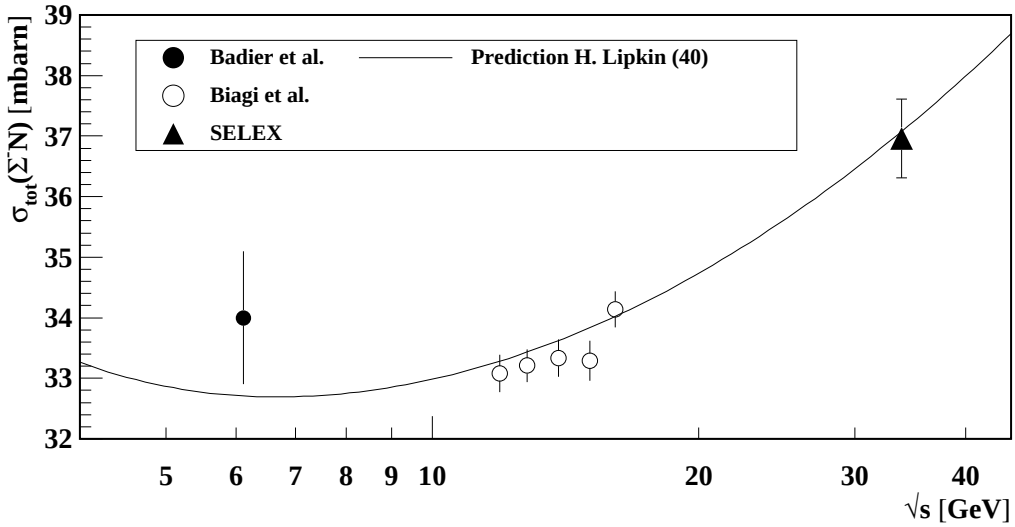

Fig. 15. Existing data for $\sigma_{\rm tot}(\Sigma^-{\rm p})$ in comparison with our results and prediction (40).

136.9 GeV/c. The SELEX total average for $\sigma_{\rm tot}(\Sigma^-{\rm N})$ provides first new data at higher energy. Figure 15 shows a compilation of data from previous experiments together with the SELEX result. Our measurement is 2.9 mbarn larger than the data point at 136.9 GeV/c from [4]. It shows the rise of $\sigma_{\rm tot}(\Sigma^-{\rm p})$ with increasing beam energy.

Overlaid to the experiment data is the prediction for $\sigma_{\rm tot}(\Sigma^-{\rm p}, {\rm p_{lab}})$ from H. Lipkin (see [36]), which is given by:

$$\sigma_{\rm tot}(\Sigma^-{\rm p}, {\rm p_{lab}}) = 19.5 \left(\frac{\rm p_{lab}}{20}\right)^{0.13} + 13.2 \left(\frac{\rm p_{lab}}{20}\right)^{-0.2} \quad (40)$$
$$\text{for } {\rm p_{lab}} > 10\,{\rm GeV/c},\ \sigma_{\rm tot} \text{ in mbarn},\ {\rm p_{lab}} \text{ in GeV/c}\ .$$

The corresponding curve in figure 15 shows good agreement between our measurement and this prediction.

It would be certainly desirable to find the Pomeron intercept for the Σ^-p cross section. But the lack of low energy data does not allow any reasonable estimate of the intercept.

9 Conclusions

The SELEX collaboration has measured the total cross sections $\sigma_{\rm tot}(\pi^-{\rm Be})$, $\sigma_{\rm tot}(\pi^-{\rm C})$, $\sigma_{\rm tot}(\pi^-{\rm Cu})$, $\sigma_{\rm tot}(\pi^-{\rm CH_2})$, $\sigma_{\rm tot}(\Sigma^-{\rm Be})$, $\sigma_{\rm tot}(\Sigma^-{\rm C})$, $\sigma_{\rm tot}(\Sigma^-{\rm Cu})$, $\sigma_{\rm tot}({\rm pBe})$ and $\sigma_{\rm tot}({\rm pC})$ in a broad momentum range around 600 GeV/c using a transmission method that was adapted to the specifics of the SELEX spectrometer. The accuracy of the results is within 0.6% - 1.5% for Be, C and CH_2 and about 17.5% for Cu.

The ratios of hadron-nucleus cross sections for Be and C show that π^--nucleus cross sections are a about factor of 0.7 lower than corresponding proton-nucleus cross sections. Furthermore, we find that the Σ^--nucleus cross sections are about a factor of 0.92 smaller than corresponding proton-nucleus cross sections.

We observe that the results for $\sigma_{\rm tot}({\rm pBe})$, $\sigma_{\rm tot}({\rm pC})$, $\sigma_{\rm tot}(\pi^-{\rm Be})$, $\sigma_{\rm tot}(\pi^-{\rm C})$ and $\sigma_{\rm tot}(\pi^-{\rm Cu})$ join smoothly corresponding cross-section data at lower energy. The good agreement of the proton-nucleus and the π^--nucleus cross sections to Glauber model calculations which include an inelastic screening correction and one adjustable parameter in the density distribution, justify the deduction of $\sigma_{\rm tot}(\Sigma^-{\rm p})$ and $\sigma_{\rm tot}(\pi^-{\rm p})$ from the nuclear cross sections.

We deduced the hadron-nucleon cross sections $\sigma_{\rm tot}(\pi^-{\rm N})$ and $\sigma_{\rm tot}(\Sigma^-{\rm N})$, which we regard as $\sigma_{\rm tot}(\pi^-{\rm p})$ and $\sigma_{\rm tot}(\Sigma^-{\rm p})$, from our nuclear data using a CH_2 – C difference and a model based ratio method. Results from the difference method have an accuracy of 8.1–9.2%, while results from the ratio method have an accuracy of 2.2–5.5%.

The total averages of all methods represent first new measurements for $\sigma_{\rm tot}(\pi^-{\rm p})$ and $\sigma_{\rm tot}(\Sigma^-{\rm p})$ at higher energy. Our result for $\sigma_{\rm tot}(\Sigma^-{\rm p})$ shows clearly a rise of this cross section with increasing beam energy, which agrees with the prediction of [36].

Our result for $\sigma_{\rm tot}(\pi^-{\rm p})$ joins nicely the high energy data of [38]. As men-

tioned in section 8.3.1, the data of [38] and our result may indicate a faster increase of the π^-p cross section than predicted by the parameterization given by the Particle Data Group in 1996.

An indication of a faster increase of the π^-p cross section compared to the pp (and $\overline{\mathrm{p}}$p) one should be verified by a high statistic measurement using a π^- beam and a hydrogen target to avoid systematic errors inherent to the method used in this experiment. In our opinion a measurement of the π^-p cross section at 600 GeV/c or higher is the only experimentally accessible case to test if the high energy behaviour of the hadronic cross section can be different from the pp and (and $\overline{\mathrm{p}}$p) one.

10 Acknowledgments

We are indebted to the Fermilab staff for the realization of this experiment. We wish to thank F. Pearsall and D. Northacker for technical support. Further, we are grateful to T. Olzanovski, V. Mallinger, U. Schwan, R. Schwan, J. Zimmer and the mechanic workshop of the Max-Planck-Institute for nuclear physics at Heidelberg for support in organizing, machining and measuring target materials. We thank B. Kopeliovich and A.V. Tarasov for theoretical support and are very grateful to G.T. Garvey, J. Pochodzalla, H.W. Siebert and M. Zavertyaev for various discussions and contributions to the analysis. Last but not least it was a pleasure for us to contact H. Lipkin about model predictions.

This project was supported in part by the Bundesministerium für Bildung, Wissenschaft, Forschung und Technologie, the Consejo Nacional de Ciencia y Tecnología (CONACyT), the Conselho Nacional de Desenvolvimento Científico e Tecnológico, the Fondo de Apoyo a la Investigación (UASLP), the Fundação de Amparo à Pequisa do Estado de São Paulo (FAPESP), the Israel Science Foundation founded by the Israel Academy of Sciences and Humanities, the Istituto Nazionale di Fisica Nucleare (INFN), the International Science Foundation (ISF), the National Science Foundation (Phy#9602178), NATO (grant CR6.941058-1360/94), the Russian Academy of Science, the Russian Ministry of Science and Technology, the Turkish Scientific and Technological Research Board (TÜBİTAK), the U.S. Department of Energy (DOE grant DE-FG02-91ER40664), and the U.S.-Israel Binational Science Foundation (BSF).

References

[1] J.L. Langland, Ph. D. thesis University of Iowa (USA) August 1995.

[2] Stuart A. Kleinfelder *et al., IEEE Transactions on Nuclear Science* Vol. 35, No. 1, February 1988.

[3] U. Dersch, Ph. D. thesis Heidelberg 1998, Germany.

[4] S.F. Biagi *et al., Nucl. Phys.* B **186** (1981) 1 - 21.

[5] G. Bellettini *et al., Nucl. Phys.* **79** (1966) 609 - 624.

[6] A.M. Schiz *et al., Phys. Rev.* D **21** (1980) 3010 - 3022.

[7] P.V.R. Murthy *et al., Nucl. Phys.* B **92** (1975) 269 - 308.

[8] Particle Data Group, C. Caso *et al., The European Physical Journal* C **3** (1998) and data on total cross sections from computer readable files from: http://pdg.lbl.gov/1998/contents_plots.html

[9] A.M. Schiz, Ph. D. thesis Yale University (USA) December 1979.

[10] Landolt Börnstein tables, Volume 7, Springer edition 1973.

[11] J. Engler *et al., Phys. Lett.* **32** B (1970) 716 - 719.

[12] A. Babaev *et al., Phys. Lett.* **51** B (1974) 501 - 504.

[13] R.J. Glauber, Boulder Lectures (1959) 315 - 413.

[14] V. Franco, *Phys. Rev.* C **6** (1972) 748 - 757.

[15] V.A. Karmanov and L.A. Kondratyuk, *JETP Lett.* **18** (1973) 266 - 268.

[16] J.P. Burq *et al., Nucl. Phys.* B **217** (1983) 285 - 335.

[17] D. Gross *et al., Phys. Rev. Lett.* **41** (1978) 217 - 220.

[18] G.G. Beznogikh *et al., Phys. Lett.* B **39** (1972) 411 - 413.

[19] A.A. Vorobyov *et al., Phys. Lett.* B **41** (1972) 639 - 641.

[20] K.J. Foley *et al., Phys. Rev. Lett.* **19** (1967) 857 - 859.

[21] L.A. Fajardo *et al., Phys. Rev.* D **24** (1981) 46 - 65.

[22] P. Jenni *et al., Nucl. Phys.* B **129** (1977) 232 - 252.

[23] R.E. Breedon *et al., Phys. Rev. Lett.* B **216** (1989) 459 - 465.

[24] N. Amos *et al., Phys. Rev. Lett.* B **128** (1983) 343 - 348.

[25] U. Amaldi *et al., Phys. Rev. Lett.* B **66** (1977) 390 - 394.

[26] N. Amos *et al., Nucl. Phys.* B **262** (1985) 689 - 714.

[27] V.D. Akopin *et al., Sov. J. Nucl. Phys.* **25** (1977) 51 - 55.

[28] I.V. Amirkhanov *et al., Sov. J. Nucl. Phys.* **17** (1973) 636 - 637.

[29] K.J. Foley *et al., Phys. Rev.* **181** (1969) 1775 - 1793.

[30] V.D. Apokin *et al., Nucl. Phys.* B **106** (1976) 413 - 429.

[31] J.P. Burq *et al., Phys. Lett.* B **109** (1982) 124 - 127.

[32] L.G. Dakhno, *Sov. J. Nucl. Phys.* **37** (1983) 590 - 598.

[33] Yu. M. Kazarinov *et al., Sov. Phys. JETP* **43** (1976) 598 - 606.

[34] C. W. De Jager *et al., Atomic Data and Nuclear Data Tables* **14** (1974) 479 - 508.

[35] A. Donnachie and P. V. Landshoff, *Phys. Lett.* B **296** (1992) 227 - 232.

[36] H. Lipkin, *Phys. Rev.* D **11** (1975) 1827 - 1831.

[37] Particle Data Group, R.M. Barnett *et al., Phys. Rev.* D **54** (1996), 191 - 192.

[38] A.S. Carroll *et al., Phys. Lett.* B **80** (1979) 423 - 427.

[39] J. Badier *et al., Phys. Lett.* B **41** (1972) 387 - 392.